

A *SPITZER* IRS STUDY OF INFRARED VARIABILITY IN TRANSITIONAL AND PRE-TRANSITIONAL DISKS AROUND T TAURI STARS

C. ESPAILLAT^{1,2}, E. FURLAN^{3,4}, P. D'ALESSIO⁵, B. SARGENT⁶, E. NAGEL⁷, N. CALVET⁸, DAN M. WATSON⁹, J. MUZEROLLE⁶

Accepted to ApJ: December 7, 2010

ABSTRACT

We present a *Spitzer* IRS study of variability in 14 T Tauri stars in the Taurus and Chamaeleon star-forming regions. The sample is composed of transitional and pre-transitional objects which contain holes and gaps in their disks. We detect variability between 5–38 μm in all but two of our objects on timescales of 2–3 years. Most of the variability observed can be classified as seesaw behavior, whereby the emission at shorter wavelengths varies inversely with the emission at longer wavelengths. For many of the objects we can reasonably reproduce the observed variability using irradiated disk models, particularly by changing the height of the inner disk wall by $\sim 20\%$. When the inner wall is taller, the emission at the shorter wavelengths is higher since the inner wall dominates the emission at 2–8 μm . The taller inner wall casts a larger shadow on the outer disk wall, leading to less emission at wavelengths beyond 20 μm where the outer wall dominates. We discuss how the possible presence of planets in these disks could lead to warps which cause changes in the height of the inner wall. We also find that crystalline silicates are common in the outer disks of our objects and that in the four disks in the sample with the most crystalline silicates, variability on timescales of 1 week is present. In addition to explaining the infrared variability described above, planets can create shocks and collisions which can crystallize the dust and lead to short timescale variability.

Subject headings: accretion disks, stars: circumstellar matter, planetary systems: protoplanetary disks, stars: formation, stars: pre-main sequence

1. INTRODUCTION

T Tauri stars (TTS) are by definition variable stars, named after their prototype T Tau. Variability in this class of objects is ubiquitous and has inspired a long history of study (e.g., Joy 1945, 1949; Rydgren et al. 1976). The majority of more recent studies have focused on their optical and near-infrared (NIR) emission. Carpenter et al. (2001) found significant variability of TTS in Orion A based on near-IR JHK 2MASS photometry. The typical timescale of variation in these TTS was on the order of days and could be explained by cool spots, hot spots, extinction, and/or changes in the mass accretion rate onto the star. Work by Eiroa et al. (2002) further supported these results. For many TTS in that study the optical and JHK photometry varied simultaneously, supporting that in most objects variability is due

to star spots and variable extinction. However, for several of the objects in that sample there is no correlation between the optical and NIR. This points to structural changes in the disk, which begin to dominate the SED in the K-band, on the order of days.

With the arrival of the *Spitzer Space Telescope* (Werner et al. 2004), more detailed studies probing the mid-IR have been possible, particularly with the Infrared Spectrograph (IRS; Houck et al. 2004) which provides simultaneous wavelength coverage between ~ 5 and 38 μm . Variations in the shape and size of the 10 μm silicate emission feature has been seen in DG Tau, XZ Tau, (Bary et al. 2009) and LRL 31 (Muzerolle et al. 2009). In the case of EX Lupi, transient changes in the dust composition of the disk have been detected with multi-epoch spectra of the silicate emission feature (Ábrahám et al. 2009).

Flux changes in the IRS spectra of disks have also been observed. Muzerolle et al. (2009) found substantial variability in LRL 31, located in IC 348, on timescales down to days. The flux of this object oscillated around a pivot point at 8.5 μm – as the emission decreased at wavelengths shortwards of the pivot point, the emission increased at longer wavelengths and vice versa. The star spots proposed to explain variability at shorter wavelengths could change the irradiation heating, but this would cause an overall increase or decrease of the flux, not an anti-correlation between the flux centered at the pivot point. Muzerolle et al. (2009) proposed that the observed “seesaw” variability was due to dynamical changes in the disk itself. In particular, changes in the height of the inner disk edge or wall located at the dust destruction radius (which emits primarily in the NIR)

¹ NSF Astronomy & Astrophysics Postdoctoral Fellow

² Harvard-Smithsonian Center for Astrophysics, 60 Garden Street, MS-78, Cambridge, MA, 02138, USA; cespaillat@cfa.harvard.edu

³ *Spitzer* Fellow

⁴ Jet Propulsion Laboratory, California Institute of Technology, Mail Stop 264-767, 4800 Oak Grove Drive, Pasadena, CA 91109, USA; Elise.Furlan@jpl.nasa.gov

⁵ Centro de Radioastronomía y Astrofísica, Universidad Nacional Autónoma de México, 58089 Morelia, Michoacán, México; p.dalessio@crya.unam.mx

⁶ Space Telescope Institute, 3700 San Martin Drive, Baltimore, MD 21218, USA; muzerol@stsci.edu

⁷ Departamento de Astronomía, Universidad de Guanajuato, Guanajuato, Gto, México 36240; erick@astro.ugto.mx

⁸ Department of Astronomy, University of Michigan, 830 Denison Building, 500 Church Street, Ann Arbor, MI 48109, USA; ncalvet@umich.edu

⁹ Department of Physics and Astronomy, University of Rochester, NY 14627-0171, USA; dmw@pas.rochester.edu

could lead to variable shadowing of the outer disk material (which emits at longer wavelengths). Indeed, the overall characteristics of the flux changes observed can be explained by models of a disk with an inner warp that leads the scale height of the inner disk to change with time (Flaherty & Muzerolle 2010).

It is important to note that the above-mentioned object, LRL 13, is surrounded by a transitional disk. Transitional disks have nearly photospheric near-IR ($1\text{--}5\text{ }\mu\text{m}$) and mid-IR ($5\text{--}20\text{ }\mu\text{m}$) emission below the median excess of Class II objects, coupled with substantial emission above the stellar photosphere at wavelengths beyond $\sim 20\text{ }\mu\text{m}$ (Strom et al. 1989). This dip in the infrared flux has been attributed to a central “hole” in the dust distribution of the disk. This has been inferred from detailed modeling of some of these transitional objects (Calvet et al. 2002, 2005; Espaillat et al. 2007b, 2008b) and confirmed with sub-millimeter and millimeter interferometric imaging (Hughes et al. 2007, 2009; Andrews et al. 2009).

Motivated by the variability observed in the transitional disk of LRL 13, we conducted a *Spitzer* IRS variability study of transitional disks and pre-transitional disks. Pre-transitional disks have significant near-infrared excesses relative to their stellar photospheres, similar to the median spectral energy distribution of disks in Taurus (D’Alessio et al. 1999), while also exhibiting the characteristics seen in transitional disks (i.e. deficits of mid-infrared flux and substantial excesses beyond $\sim 20\text{ }\mu\text{m}$). This indicates a gapped disk structure where the inner disk is separated from the outer disk. Sub-millimeter and millimeter interferometric imaging (Andrews et al. in prep; Andrews et al. 2009; Piétu et al. 2006) has confirmed the location of the wall of the outer disk inferred from SED modeling for a few pre-transitional disks (e.g. LkCa 15, UX Tau A, Rox 44). The near-IR emission of these objects is due to dust in an optically thick inner disk, a result obtained by using the “veiling” (Hartigan et al. 1989) of near-infrared spectra (Espaillat et al. 2008a, 2010).

Here we perform detailed modeling of the broad-band spectral energy distributions of the 14 transitional and pre-transitional disks in our sample at different epochs. We take into account the effect of shadowing by the inner disk on the outer disk by employing the irradiated accretion disk models of D’Alessio et al. (2006) with the modifications to include shadowing presented in Espaillat et al. (2010). Our work adds to the number of detailed modeling efforts of disk variability in the literature which have found some success in reproducing the observations by varying the height of the inner disk wall (Juhász et al. 2007; Sitko et al. 2008). Juhász et al. (2007)’s study of the UX Ori-type star SV Sep came to the conclusion that the variability in the optical and near-IR emission could be explained by changing the height of the inner disk edge, but they were unable to simultaneously fit the variability from the IR out to $100\text{ }\mu\text{m}$ using a self-shadowed disk. Sitko et al. (2008) reported the variability of two Herbig Ae stars between $1\text{--}5\text{ }\mu\text{m}$, the region dominated by the inner disk wall, and could explain this change by varying the height of the inner disk edge. However, this work did not have data at longer wavelengths and so could not test if these models fit the emission from the outer disk.

The advantage of our study over previous works is the quality of the data and the simultaneous wavelength coverage ($5\text{--}38\text{ }\mu\text{m}$) provided by *Spitzer* IRS. Thus we are able to present the largest and most detailed modeling study of variability in disks around TTS to date. We find that we can explain the variability of most of the pre-transitional disks in the sample by changing the height of the inner disk wall and thus the extent of its shadow on the outer disk, thereby affecting the resulting emission from the outer disk. We also find that the objects in the sample with the largest amounts of crystalline silicates in their disks exhibit variability on the shortest timescales observed in this study.

2. SAMPLE SELECTION

Our sample of 14 objects was chosen to include bright transitional and pre-transitional disks in Taurus and Chamaeleon, two nearby 1–2 Myr old star-forming regions with low extinction that were well covered by a *Spitzer* guaranteed-time observing (GTO) program (Manoj et al., submitted; Furlan et al. 2006; Kim et al. 2009). For each of our 14 objects we obtained a pair of general observer (GO) observations taken within 1 week of each other. When combined with the GTO data, these observations give us baselines of $\sim 3\text{--}4\text{ yr}$ and $\sim 1\text{ wk}$.

We included the well-studied and previously modeled transitional disks CS Cha, DM Tau, and GM Aur (Espaillat et al. 2007b; Calvet et al. 2005) and the pre-transitional disks LkCa 15 and UX Tau A (Espaillat et al. 2007a). We also included other transitional and pre-transitional disks in Chamaeleon (T25, T35, T56, SZ Cha) which had been identified by Kim et al. (2009). Four objects in our sample were chosen based on analysis conducted in Furlan et al. (2009). In that work, we compared the observed equivalent width of the $10\text{ }\mu\text{m}$ silicate emission feature and the SED slope between 13 and $31\text{ }\mu\text{m}$ against a grid of disk models. RY Tau, IP Tau, CR Cha, and WW Cha were four of the many objects that fell outside of range of EW($10\text{ }\mu\text{m}$) and $n_{13\text{--}31}$ covered by the full disk model grid. One explanation proposed by Furlan et al. (2009) and Espaillat (2009) to explain these outliers was that these disks are actually pre-transitional disks with smaller gaps than had been previously observed. Therefore, we included these objects in the sample based on their potential for being pre-transitional disks. ISO 52 is the only object in our sample which could be explained by the full disk model grid presented in Furlan et al. (2009). However, we chose to include this object in our variability study because qualitatively its GTO IRS spectrum resembled what would be expected from a pre-transitional disk with a small gap (see Figure 12 in Espaillat et al. 2010). Except for CS Cha, the objects in our sample are thought to be single stars and so the holes and gaps in our objects indicate the likely presence of planets (see discussion in Espaillat et al. 2008a, 2010).¹⁰

¹⁰ Even in the case of the spectroscopic binary of CS Cha, the 38 AU hole is too large to be cleared out by the binary system alone. A binary system with a circular orbit can clear a hole twice the size of the semi-major axis; a binary with an eccentricity of 0.8 can clear out a region 3.5 times the semi-major axis (Artymowicz & Lubow 1994; Pichardo et al. 2005; Aguilar et al. 2008). Since the separation of the binary in CS Cha is $\sim 4\text{ AU}$ (Guenther et al. 2007), the binary should clear only a region up to 14 AU.

3. DATA REDUCTION

3.1. Observations

Here we present three *Spitzer* IRS spectra for each of our targets (Table 1). The first spectra were obtained through IRS GTO in Program 2 (PI: Houck) and have been previously presented elsewhere (Manoj et al., submitted; Furlan et al. 2006, 2009; Kim et al. 2009). The last two spectra for each target were obtained in GO Program 50403 (PI: Calvet). For consistency, we have re-reduced the GTO data in the same way we reduce the GO data (see § 3.2). We note that we also searched the *Spitzer* archive for all other IRS observations of objects in our sample. We reduced those data as we did our GTO and GO data and comment further on these additional spectra in the Appendix.

All of the GO observations were performed in staring mode using the low-resolution modules (Short-Low (SL) and Long-Low (LL)) of IRS, spanning wavelengths from 5–14 μm and 14–38 μm , respectively, with a resolution $\lambda/\delta\lambda \sim 90$. The Chamaeleon GTO spectra were obtained in staring mode as well while the Taurus GTO spectra were obtained in mapping mode with 2×3 step maps (2 parallel and 3 perpendicular to the slit) on the target. Most of the GTO spectra use the SLLL configuration. The exceptions are RY Tau, CR Cha, and WW Cha which were taken with the SL module and the high-resolution modules Short-High (SH) and Long-High (LH), which cover 10–19 μm and 19–37 μm , with $\lambda/\delta\lambda \sim 600$. We note that in the case of DM Tau, two GTO spectra were obtained in Program 2 and are listed in Table 1 as GTO1 and GTO2. Throughout this paper, we only show the GTO2 spectrum since it was taken in staring mode, as were our GO observations. In addition, the SL spectrum has a higher SNR in the GTO2 observation due to a longer integration time. We note that the GTO1 spectrum is equivalent to the GTO2 spectrum (i.e. flux, shape) within the uncertainties of the observations.

3.2. Extraction and Calibration of Spectra

Details on the observational techniques and general data reduction steps, including bad pixel identification, sky subtraction, and flux calibration, can be found in Furlan et al. (2006) and Watson et al. (2009). Here we provide a brief summary. Each object was observed twice along the slit, at a third of the slit length from the top and bottom edges of the slit. Basic calibrated data (BCD) with pipeline version S18.7 for both the GTO and GO observations were obtained from the *Spitzer* Science Center. With the BCDs, we extracted and calibrated the spectra using the SMART package (Higdon et al. 2004). Bad and rogue pixels were corrected by interpolating from neighboring pixels. For the low-resolution spectra, the data were sky subtracted using the sky emission in the off-target nods except in the cases of CS Cha GO1, IP Tau GO 1, and LkCa 15 GO 2 where the off-target orders were used in order to minimize over-subtraction of H I from the sky background at $\sim 20 \mu\text{m}$. For the GTO SH and LH modules, no background subtraction was performed and so the emission of these targets could be slightly overestimated, particularly in LH since the slit is larger. However, the targets are much brighter than the background, and so the emission from the disks should clearly dominate in the mid-IR. After sky subtrac-

tion, the low-resolution spectra were extracted from the 2D spectral images using a tapered column which varies with the width of the IRS point-spread function. For the SH and LH modules, a full slit extraction was performed. To flux calibrate the observations we used spectra of α Lac (A1 V) for the low-resolution modules and ξ Dra (K2III) for the high resolution modules. We performed a nod-by-nod division of the target spectra and the α Lac or ξ Dra spectra and then multiplied the result by a template spectrum (Cohen et al. 2003). The final spectrum was produced by averaging the calibrated spectra from the two nods. For the 2×3 maps, only the central map positions were used for the final spectrum. The high-resolution data were rebinned to same sampling as the low-resolution data. Our spectrophotometric accuracy is 2–5% estimated from half the difference between the nodded observations. We note that there are artifacts in the T25 GO1, ISO 52 GO1, T56 GO1, and CR Cha GTO spectra at $\sim 9 \mu\text{m}$, $\sim 7 \mu\text{m}$, $\sim 15 \mu\text{m}$, and $> 35 \mu\text{m}$, respectively. These spikes are due to additional bad pixels not captured by the bad pixel and rogue masks used in our data reduction. For clarity, we manually mask these artifacts from the spectra. The final spectra used in this study are shown in Figures 1, 2, and 3.

3.3. Uncertainties due to Mispointing

Apparent variability could also be the effect of mispointings, which would cause loss in flux especially in SL, which is the module with the narrowest slit width. PCRS peak-up, which we used for our GO observations, yields a pointing accuracy of $0.4''$ (1-sigma radial rms); this is just slightly less than the accuracy for blind pointing ($0.5''$); however, note that earlier in the mission the blind pointing of *Spitzer* was only accurate to $< 1''$. According to a detailed study in Swain et al. (2008), a $0.4''$ pointing offset in SL1 causes a drop in flux of about 7%, with a slight (1–2%) dependence on wavelength. Therefore, if we observe a flux variation $\geq 10\%$ that fluctuates with wavelength more than on the few percent level, we can most likely exclude mispointing as the cause of the variability.

The GTO observations did not use peak-ups. However, the GTO data of our Chamaeleon objects were taken later in the mission, when the blind pointing of *Spitzer* was improved. The objects in our sample that could be affected by some mispointing are the Taurus GTO observations, taken in 2004 February. They were obtained with blind pointing in mapping mode; the spectra presented here are extracted from the central map positions. For IP Tau, DM Tau GTO1, and LkCa 15, the SL and LL spectra match at $14 \mu\text{m}$, which argues against mispointing; since the SL and LL slits are perpendicular to each other, mispointings should affect one module more than the other, resulting in an offset. There were small (5%) offsets between SL and LL for DM Tau GTO2, GM Aur and UX Tau A, with SL lower than LL, suggesting small mispointings. RY Tau likely suffered from larger mispointing, since SH is lower than SL and LH by 20–30% (the mispointing relative to SL is more difficult to determine, given that part of SL1 in the GO spectra is saturated); also, compared to the GO data, the SL spectrum appears low. Overall, the GTO spectrum of RY Tau is quite uncertain, but the other GTO observations should have a pointing accuracy of $0.5''$ or better. In

order to account for the mispointing discussed here we scale the SL spectra upward so that the SL and LL spectra match. We note that the high-resolution modules SH and LH are much less affected by small mispointings, since the slits are wider than for the low-resolution modules.

We note that none of the other GTO or GO observations were mispointed. Aside from those observations discussed above, there is no mismatch between SL and LL, so we can be confident that the observations are well pointed and that therefore both the SL and LL slits contain the full flux of the object. As an additional check, we find that the sources are located within $\sim 1''$ of each other in the SL and LL slits amongst the GTO, GO1, and GO2 observations, further evidence that these sources were well-centered in the slit. We note that at $\sim 14\mu\text{m}$ the SL module ends and the LL module begins. Given that several of our objects have large holes and gaps, the emission of the outer wall begins to dominate at $15\text{--}20\mu\text{m}$, coinciding with where SL ends and LL starts.

We also overlaid the IRS slit positions for each AOR on 2MASS K-band images to check for anomalous behavior. In WW Cha GO1 and GO2 both of the modules were mispointed due to an error in the coordinates (the declination was off by $\sim 1''$). Judging from the overlay, the LL module was more off-target than the SL module and the mispointing is more along the spatial direction of the SL slit, but it is difficult to tell how much flux was lost. We note that in the GO observations of SZ Cha, two faint objects entered the SL and LL slits at $5.3''$ and $12.5''$ from the target. However, it is known that these two objects are not members of Cha I and are likely very faint at mid-IR wavelengths (Luhman 2007). Therefore, SZ Cha dominates the emission in the GO spectra. In the GTO observations of ISO 52 a faint object is present in the LL slit $8.5''$ from the target. Due to the different orientation of the IRS slit positions in the GO observations, this object is not present in the LL slit in this epoch. However, this object is much fainter than ISO 52, with a magnitude of about 14 in the 3.6 and $4.5\mu\text{m}$ IRAC bands (K. Luhman, 2010, private communication), and so we can conclude that ISO 52 dominates the emission seen in its GTO spectrum.

4. ANALYSIS

4.1. Flux Variability

It is evident from the IRS spectra of our pre-transitional (Figures 1 and 2) and transitional objects (Figure 3) that there is some variability in their fluxes. Here we quantitatively discern if there is true variability in the sample and then qualitatively discuss the overall behavior of the variability that is present.

Figures 4–9 illustrate the change in flux seen in an object in our sample between different epochs. The differences in flux between the GTO and GO1 spectra are shown in Figures 4–6. (Note: the same analysis for UX Tau A and T35 is plotted in Figure 7). The difference in flux (δF_λ) is plotted in terms of the percentage difference in emission between the GTO and GO1 data relative to the GTO data. The error bars in the figures correspond to the uncertainties in the observations. Except for the cases of DM Tau and T25 (where $\delta F_\lambda \sim 0$), we observe significant variability outside of the observational

uncertainties in each of the targets between the GTO and GO1 observations, which were taken more than a year apart. We performed the same analysis comparing the GO1 and GO2 spectra, which were taken about one week apart, and we only see variability on these timescales in four objects: UX Tau A (Figure 4), ISO 52, T56 (Figure 7), T35 (Figure 4). In Figures 8 and 9 we show that the rest of the objects in our sample do not vary significantly between the GO1 and GO2 epochs.

In many of the pre-transitional targets, the flux clearly oscillates around a pivot wavelength (Figure 4). As the short wavelength emission decreases, the emission at longer wavelengths increases and as the short wavelength emission increases, the emission at longer wavelengths decreases. The spectra of LkCa 15 can be taken as representative of this group of objects. In Figure 4 the flux of its GO1 spectrum is $\sim 10\%$ lower than the GTO spectrum at wavelengths $< 8\mu\text{m}$. The fluxes of the two spectra are the same around $\sim 10\mu\text{m}$, but the GO1 spectrum is higher beyond that point. In the other objects mentioned above, the overall behavior is similar while the pivot wavelength and magnitude of the flux change can vary from object to object. UX Tau A does not display this seesaw behavior between the GTO and GO1 spectra (Figure 7), but it does between the GO1 and GO2 spectra (Figure 4). We point out that while the RY Tau GTO and WW Cha GO observations were mispointed, that should have resulted in an decrease of flux at all wavelengths relative to the GO and GTO observations, respectively. However, we see flux losses at some wavelengths while flux gains at others, indicating that there is true variability in these objects, but we cannot accurately constrain the difference in the flux or the pivot wavelength due to the mispointing.

Whether or not this seesaw behavior is present in the other pre-transitional objects in the sample is unclear (Figure 5). The GO1 spectrum of CR Cha has less emission than the GTO spectrum shortwards of $\sim 6\mu\text{m}$, but substantially more at longer wavelengths. Due to the artifacts in the GTO spectrum $> 35\mu\text{m}$ discussed in § 3, we cannot confidently tell whether or not the GTO and GO spectra agree at these wavelengths. In IP Tau the flux at $\lambda < 7\mu\text{m}$ is about the same, but it is lower for the GO1 spectrum at longer wavelengths. For T56, the emission in the GO1 spectrum is higher than the GTO spectrum beyond $\sim 20\mu\text{m}$. It appears that the flux in the GO1 spectrum is lower at $< 20\mu\text{m}$, but the SNR is too poor $< 7\mu\text{m}$ to tell if this holds at the shortest wavelengths. In T35, when comparing the GO1 and GO2 spectra, the flux is the same $< 7\mu\text{m}$, but the GO2 spectrum has less emission beyond that. Again, the spread in uncertainties is large in T35 because of the poorer SNR.

The behavior observed in the transitional disks is displayed in Figure 6. GM Aur has the seesaw behavior seen in LkCa 15, where the pivot is at $\lambda \sim 18\mu\text{m}$. In CS Cha, only the flux of the $10\mu\text{m}$ silicate emission feature changes substantially between the GTO and GO1 spectra. DM Tau and T25 have no discernible variability.

The four objects in our sample which vary on 1 wk timescales display behavior that could be classified as seesaw-like as already described above, but they also exhibit additional behavior (Figure 7). UX Tau A's GO1 spectrum is weaker at all wavelengths relative to the

GTO spectrum, indicating that the emission of this object has decreased with time. The spread in uncertainties is large in ISO 52, T56, and T35 because of poor SNR; however, it appears that the ISO 52 and T56 spectra diverge beyond $\sim 20 \mu\text{m}$ between the GO1 and GO2 spectra and that the T35 spectra diverge shortwards of $\sim 10 \mu\text{m}$ between the GTO and GO1 spectra.

4.2. Disk Model

Using disk models, we attempt to reproduce the SED variability observed in Figures 1–3. The models used here are those of D’Alessio et al. (1998, 1999, 2001, 2005, 2006). We refer the reader to those papers for details of the model and to Espaillat et al. (2010) for a summary of how we fit the SEDs of pre-transitional and transitional disks in particular.

A full disk model has an irradiated accretion disk with a sharp transition at the dust sublimation radius. We model this transition as a frontally illuminated wall which dominates the near-IR emission. Pre-transitional disks have a gap in the disk. They have an inner disk separated from an outer disk by the gap. The optically thick inner disk also has a sharp transition at the dust sublimation radius, as seen in full disks, which we model as an inner wall. In the subsequent modeling analysis, we do not include the contribution to the SED from the inner disk behind this wall since previous work has shown that the inner wall dominates the emission at these shorter wavelengths. There is another wall located where the outer disk is inwardly truncated (i.e. the outer edge of the gap) and this outer wall dominates the SED emission from $\sim 20\text{--}30 \mu\text{m}$. Behind this wall, there is an outer disk which dominates the emission beyond $\sim 40 \mu\text{m}$. Since transitional disks have holes in their disks, they do not have the inner wall seen in pre-transitional disks. When modeling transitional disks, we include the outer wall and outer disk described above. In both pre-transitional and transitional disks, the gap or hole sometimes contains a small amount of optically thin dust which dominates the contribution to the $10 \mu\text{m}$ silicate emission feature. We calculate the emission from this optically thin dust region following Calvet et al. (2002). We note that in the case of the pre-transitional disks, the inner optically thick disk will cast a shadow on the outer disk and here we include the effect of this shadowing on the outer wall following Espaillat et al. (2010). In short, since the star is a finite source, there is both a penumbra and umbra on the outer wall. In the umbra, the wall is not illuminated and in the penumbra, the wall is partially illuminated. Above the penumbra, the wall is fully illuminated. Refer to the Appendix of Espaillat et al. (2010) for more details.

4.2.1. Stellar Properties

Table 2 lists stellar properties for our sample which are relevant for the disk model. We note that the stellar properties of our objects are based on optical and near-infrared data which are not contemporaneous with the IRS spectra analyzed in this work. If the star’s properties change over time this can result in uncertainties in the input stellar parameters and hence the disk properties derived here.

Spectral types for our objects are from the literature and the temperature for the spectral type listed

in Table 2 was taken from Kenyon & Hartmann (1995). The stellar properties for our sample (L_* , M_* , R_*) are from the HR diagram and Siess et al. (2000) tracks. When U-band photometry was available, the mass accretion rates were derived in this work using U-band data and the relation in Gullbring et al. (1998). Extinction corrections were made by matching V-, R-, I-band, and 2MASS photometry to photospheric colors from Kenyon & Hartmann (1995). The spectra were dereddened with the Mathis (1990) dereddening law. The distance adopted for Taurus is 140 pc (Bertout et al. 1999) and for Chamaeleon this is 160 pc (Whittet et al. 1997).

4.2.2. Disk Properties

Table 3 lists the disk properties of our sample. When parameters are specific to only one epoch, this distinction is made in the table (see table footnote). We assume that the inclination of the disk is 60 degrees, unless a measurement could be found in the literature. T_{wall} is the temperature at the surface of the optically thin wall atmosphere. The temperature of the inner wall (T_{wall}^i) is typically held fixed at 1400 K (except in the cases of UX Tau A and T35 which will be addressed in the Appendix). The temperature of the outer wall (T_{wall}^o) is varied to fit the SED best. The radius of the wall (R_{wall}) is derived using T_{wall} following Equation 2 in Espaillat et al. (2010). The heights of the walls (z_{wall}) and the maximum grain sizes (a_{max}) are adjusted to fit the SED. The parameters of the outer disk are also varied to fit the SED. These include the viscosity parameter (α) and the settling parameter (ϵ ; i.e. the dust-to-gas mass ratio in the upper disk layers relative to the standard dust-to-gas mass ratio). \dot{M}_{disk} is calculated according to Equation 38 in D’Alessio et al. (1998) and it is proportional to \dot{M}/α . We adopt an outer disk radius of 300 AU for all of our disks.

4.2.3. Dust Opacities

As discussed in Espaillat et al. (2010), the opacity of the disk has important consequences on the resulting SED. The opacity is affected by the sizes of the dust grains and the composition of the dust used. The grain size distribution used in the models follows the form $a^{-3.5}$ where a varies between a_{min} and a_{max} (Mathis et al. 1977). We assume the grains are spherical and note that while irregularly shaped grains may have different opacities from spherical grains (Min et al. 2007), it is outside the scope of this work to constrain the shape of the dust grains. Throughout the disk, a_{min} is held fixed at $0.005 \mu\text{m}$. In the walls, a_{max} is varied to achieve the best fit to the SED. We try maximum grain sizes between $0.25 \mu\text{m}$ and $10 \mu\text{m}$. The wall emission is primarily optically thick, but also has an optically thin component from the wall atmosphere which contributes to the silicate emission features. Smaller grain sizes lead to a strong, narrow $10 \mu\text{m}$ silicate emission feature while larger grain sizes produce wider and less prominent emission features (see Figure 3 in Espaillat et al. 2007b). In the outer disk, there are two dust grain size distributions in order to simulate dust growth and settling (see D’Alessio et al. 2006, for more details). In the upper disk layers, $a_{\text{max}}=0.25 \mu\text{m}$ and in the disk mid-plane the maximum grain size is 1 mm (D’Alessio et al.

2006). For the dust composition of the inner wall we follow D’Alessio et al. (2005) and Espaillat et al. (2010) in adopting silicates with a dust-to-gas mass ratio (ζ_{sil}) of 0.0034. We note that only silicates exist at the high temperatures at which the inner wall is located. There are other types of dust such as metallic iron that can exist at high temperatures (Pollack et al. 1994). However, here we adopt a dust composition consistent with the one proposed by Pollack et al. (1994) for accretion disks.

We perform a more detailed dust composition fit for the silicates in the outer wall and disk than done in our previous works. The motivation is that for a variability study trying to trace small changes in the flux, it is important to isolate the continuum emission of the disk. By fitting the silicate dust features seen in the IRS spectrum as closely as possible, one can then more clearly see the effect of changing the disk continuum. Here we adopt a dust-to-gas mass ratio (ζ_{sil}) of 0.0034 for the silicates in the outer wall and disk and explore silicate dust mixtures incorporating olivines, pyroxenes, forsterite, enstatite, and silica. (We note that throughout this work we are referring to amorphous material of olivine or pyroxene stoichiometry when using the terms “olivine” and “pyroxene.”) We list the derived mass fractions in Table 4.

The optical constants used for olivines and pyroxenes come from Dorschner et al. (1995). We calculate the opacities assuming segregated spheres and Mie theory for the adopted dust grain size distribution. For an explanation of how the forsterite opacity was computed, see the discussion by Poteet et al. (2010).

We also calculated the opacity for enstatite. We adopt optical constants for enstatite from Huffman & Stapp (1971) and Egan & Hilgeman (1977), crystalline bronzite at 300K from Henning & Mutschke (1997), the three crystalline axes of orthoenstatite from Jaeger et al. (1998), and crystalline hypersthene from Jaeger et al. (1994, Sample 1S) for the 0.1–0.5, 0.533–1.105, 6.7–8.4, 8.7–98, and 98–8000 μm wavelength regimes, respectively. The optical constants from Jaeger et al. (1994) were modified to match the values from Jaeger et al. (1998) as was done for forsterite as described by Poteet et al. (2010). Beyond 585 μm , the real part of the index of refraction, n , was chosen to be a constant value equal to the value of n at 585 μm obtained by modifying the Jaeger et al. (1994) n values, and the imaginary part of the index of refraction, k , was determined by scaling a $1/\lambda$ curve to the value of k , at 585 μm from the modified Jaeger et al. (1994) values. The absorption opacity was then computed from these optical constants by CDE theory (Bohren & Huffman 1983). The scattering opacity is assumed to be zero.

Finally, we compute the opacity for silica. We adopt optical constants from the following sources for silica. Between 0.05 to 0.15 μm , alpha quartz from Palik (1985) is used. From 3–8 μm , k comes from k_{abs} for amorphous silica from Palik (1985). For k between 0.15 and 3 μm , k is interpolated between its values at 0.15 and 3 μm . From 0.15 to 5.5 μm , n comes from Palik (1985) for alpha quartz. Between 8 and 30 μm , the n and k values for beta quartz at 975 K from Gervais & Piriou (1975) are used. From 50–333 μm , both n and k are from Loewenstein et al. (1973) for alpha quartz at room temperature. The value of n at 333 μm was kept con-

stant to 8000 μm . For k , a $1/\lambda$ curve fit to the value of k at 333 μm was used. To compute the absorption opacity, we employed CDE at all wavelengths except 8 to 40 μm . Between 8 to 40 μm the absorption opacity was for annealed silica from Fabian et al. (2001). The scattering opacity at all wavelengths is assumed to be zero.

In addition to silicates, for each of the disks, we add organics and troilite to the dust mixture following Espaillat et al. (2010) with $\zeta_{org} = 0.001$ and $\zeta_{troi} = 0.000768$ and sublimation temperatures of $T_{org} = 425$ K and $T_{troi} = 680$ K. We include water ice as well with a sublimation temperature of 110 K. Unless otherwise noted, we use $\zeta_{ice} = 0.00056$. Optical constants for organics, troilite, and water ice are adopted from Pollack et al. (1994), Begemann et al. (1994), and Warren (1984). In objects where we include optically thin dust within the hole or gap, the silicate dust composition is listed in Table 5. The abundances of silicates, organics, and troilite in the optically thin dust region are given in the subsequent sections. We do not include ice in the optically thin region since the temperatures here are high enough for it to have sublimated.

4.3. SED Modeling

Here we provide an overview of our modeling results. In the Appendix, we describe in detail the modeling conducted in this study for each individual object.

4.3.1. Disk Structure

We can explain most of the seesaw variability observed in the pre-transitional disks by changing the height of the inner disk wall. (We note that other possible explanations including changes in the stellar and disk properties have not been explored here.) In the pre-transitional disks of LkCa 15, SZ Cha, and UX Tau A we can reproduce the seesaw variability by changing the height of the inner disk wall by $\sim 22\%$, 33% , and 17% respectively (Figure 10). When the inner wall is taller, the emission at the shorter wavelengths where the wall dominates the emission is higher; there is also a larger shadow on the outer wall and hence the emission seen from the outer wall is less and the IRS spectrum is lower. Correspondingly, when the inner wall is lower there is less near-IR emission and the shadow on the outer wall is smaller and so we see more emission from the outer wall longwards of 20 μm . The 10 μm silicate emission in LkCa 15 and SZ Cha does not change. This emission is dominated by small dust in the optically thin region. UX Tau A does not have a discernible 10 μm silicate emission feature.

Because of uncertainties introduced to the observations by mispointing, we do not attempt to reproduce the variability seen in RY Tau (Figure 11). However, we can fit the SED of RY Tau with an 18 AU gap which contains some optically thin dust. In the case of WW Cha (Figure 12), due to the fact that the GO observations were significantly mispointed and that we do not have a mass accretion rate estimate, we do not attempt to model its disk here.

We also do not have a mass accretion rate for ISO 52 (Figure 13). However, these observations were well pointed and for the purposes of reproducing the general trend seen in the variability, we assume a typical value (see the Appendix for more details). In this object, we

need to increase the height of the inner wall by $\sim 400\%$ between the GTO and GO epochs to explain the observed variability. Assuming that our assertion that the inner wall height is varying is correct, this is by far the largest change in wall height seen in the sample.

CR Cha has a substantial change in slope at $\sim 6 \mu\text{m}$ (Figure 14), from which one could infer that there is either a substantial change in the temperature of the wall or a change in the nature of the emission from optically thick to optically thin. We find that CR Cha is best explained with a pre-transitional disk model in the GTO observations and either a pre-transitional or transitional disk model in the GO observations. See the Appendix for more details and § 5.1.3 for a discussion.

In the pre-transitional disks of IP Tau, T56, and T35, we can reasonably reproduce the emission within the uncertainties of the observations by varying the height of the inner disk wall by 17%, 50%, and 20%, respectively (Figure 15). In addition to varying the height of the inner wall, we also had to change the amount of dust in the optically thin regions of IP Tau and T56 in order to reproduce the variability in the $10 \mu\text{m}$ silicate emission feature.

We also modeled the transitional disks in the sample (Figures 16 and 17). GM Aur displays seesaw behavior. To fit it we vary the amount of optically thin dust in the hole and have to change the height of the outer wall as well. In CS Cha, only the $10 \mu\text{m}$ silicate emission changes between epochs and to fit this variability we alter the amount of dust in the optically thin region. In DM Tau and T25 there is no variability and there is no evidence for significant amounts of dust in their holes.

There is some variability in the pre-transitional disks which we cannot explain by changing the height of the inner disk wall. The GO2 spectrum of T35 has a change in slope at $\sim 7 \mu\text{m}$ which we could not explain with the disk models presented here. We have no obvious explanation for this but speculate it could be related to the high temperature derived for the inner disk wall (1800 K). In UX Tau A, the overall emission from the disk has decreased with time (i.e. the GO spectra have less emission than the GTO spectra). While we do not try to fit this decrease with models, it can possibly be attributed to a decrease in the luminosity at the bands where the disk absorbs stellar radiation, most likely due to star spots (Skrutskie et al. 1996), or an overall decrease in the accretion luminosity of the disk, most likely from a change in the mass accretion rate by a factor of about 3. We also analyzed an additional SHLH spectrum from the *Spitzer* archive (see Appendix for more details). This spectrum has substantially lower emission at $\lambda > 13 \mu\text{m}$ (Figure 18). We can fit the SHLH spectrum using an inner wall with a temperature of 1800 K. This hotter inner wall is closer to the star and leads to a larger shadow on the outer wall. Given that we do not have simultaneous data at shorter wavelengths, we cannot test if this wall fits the SED at $\lambda < 10 \mu\text{m}$ at the time the SHLH spectrum was taken.

4.3.2. Dust Composition

As a result of trying to reproduce the variability observed in our sample, in this study we also performed fitting of the silicate emission features visible in the IRS spectra, deriving the mass fraction of amorphous and

crystalline silicates in the outer wall and the optically thin regions (Tables 4 and 5). (We refer the reader to Figure 1 of Watson et al. (2009) for the positions of the strongest features of crystalline silicates visible in IRS spectra.) We do not attempt a detailed χ^2 fitting since it would be too computationally expensive to do so with our disk code. Thus, the derived mass fractions in Tables 4 and 5 should be taken as representative of a dust composition that can reasonably explain the observed SED. We refer the reader to Sargent et al. (2009) for a review of the typical degeneracies of dust fitting. In short, large grains of amorphous olivine and amorphous pyroxene composition are the most degenerate, in the sense that one of these components could be replaced by the other and a similar fit would be found. Enstatite and forsterite are also somewhat degenerate at cooler temperatures. Another caveat, which was noted earlier, is that the shapes of the grains in the disk are not well known. We leave it to future work to further constrain the mass fractions of silicates in these disks.

For the inner wall of our objects, the silicate composition consisted solely of amorphous olivines. However, since the inner wall does not produce significant $10 \mu\text{m}$ silicate emission in the objects in this study, we have no way to distinguish between pyroxene and olivine silicates in the inner wall. Also, while we included crystalline silicates in the disk behind the outer wall, it is the outer wall that dominates the emission at the longer IRS wavelengths. Because of these previous two points, here we only discuss the composition of silicates in the optically thin dust region and the outer wall.

Most of the absorption and emission of the outer walls in our sample are dominated by amorphous silicates (Table 4). The exception is T35 which is dominated by crystalline silicates ($\sim 60\%$). The optically thin region also tends to be dominated by amorphous silicates with typically $\sim 10\%$ or less of crystalline silicates. This is not the case in T56 which contains $\sim 25\%$ crystalline silicates. Of the three crystalline silicates studied in this work, we are more likely to see forsterite rather than enstatite and silica in the optically thin region (Table 5). Comparing the optically thin region and outer wall in objects that have both, it appears that silica is more likely to be present in the outer wall. Relative to the optically thin region, we find more crystalline silicates in the outer walls of T56, SZ Cha, and LkCa 15 and less for CS Cha and GM Aur. The amount of crystalline silicates in CR Cha and IP Tau is the same between both regions. RY Tau has no evidence for significant amounts of crystalline silicates in its disk.

The results from the dust fitting performed in this work are in reasonably good agreement with the detailed dust fitting conducted by Sargent et al. (2009) which used a two-temperature model. The objects that the two samples have in common are DM Tau, GM Aur, IP Tau, and LkCa 15. Both works find that these four disks are dominated by amorphous silicates and that there are relatively few crystalline silicates present. Furthermore, olivine silicates dominate the inner parts of the disk that contribute to the $10 \mu\text{m}$ emission.

5. DISCUSSION

5.1. Linking Infrared Variability to Disk Structure

Understanding the underlying causes of the variability observed in this sample depends upon the physical locations in the disk from which the changes in flux arise. Given that the sample was chosen to include pre-transitional and transitional disks, the nature of these objects will necessarily play a key role in this. The disk structures of LkCa 15, UX Tau A, GM Aur, and RY Tau have been independently confirmed. LkCa 15, UX Tau A, and GM Aur have been imaged with millimeter interferometers and large cavities in their disks have been observed (Andrews et al. in prep; Piétu et al. 2006; Hughes et al. 2009). Near-infrared spectra have confirmed that the inner disks of LkCa 15 and UX Tau A are optically thick while the inner disk of GM Aur is optically thin (Espaillat et al. 2010). Millimeter interferometric imaging of RY Tau by Isella et al. (2010) detects two spatially resolved peaks, an indicator of a disk hole, whose separation translates to a cavity that is consistent with the 18 AU gap inferred from the SED modeling in this work. For the other objects in the sample, the disk structure is inferred solely from SED modeling. Millimeter interferometry and near-IR data are needed to confirm that there are cavities in these disks and to probe if the inner disk is optically thick. However, the IRS spectra of SZ Cha, WW Cha, and T56 are reminiscent of LkCa 15, suggesting that they are gapped disks as well. Likewise, T35 resembles UX Tau A. CS Cha, DM Tau, and T25 have large deficits of flux which are strong indicators of inner disk holes, as seen in GM Aur.

It follows that one can roughly divide the disk into two regions – inner (inner wall and/or optically thin dust region) and outer (outer wall and outer disk). Interestingly, the only disks that do not display variability in our sample are the transitional disks DM Tau and T25 whose inner regions do not contain substantial amounts of small dust. DM Tau’s inner hole is relatively devoid of small dust and T25’s inner region contains only $10^{-13} M_{\odot}$. In contrast, the transitional disks of GM Aur and CS Cha have about ten times more small dust within their optically thin inner cavities than the transitional disks of DM Tau and T25. We can infer that there is not enough material in the inner regions of DM Tau and T25 to lead to significant variability. Objects in the sample that have a notable amount of material in their inner region do vary.

5.1.1. Inner Wall

We attempted to understand the variability seen in our sample by fitting the SED with disk models. In the pre-transitional disks of LkCa 15, SZ Cha, UX Tau A, IP Tau, T56, and T35 we can reasonably reproduce the emission between 5–38 μm within the uncertainties by varying the height of the inner disk wall by 22%, 33%, 17%, 17%, 50%, and 20%, respectively (Figures 10 and 15). When the inner wall is taller, the emission at the shorter wavelengths is higher since the inner wall dominates the emission at 2–8 μm . The taller inner wall casts a larger shadow on the outer disk wall and we see less emission at the wavelengths beyond 20 μm where the outer wall dominates. When the inner wall is shorter, the reverse occurs. ISO 52 is an extreme case. Its inner wall height has to change by 400% to explain the observed variability (Figure 13).

We did not attempt to fit the variability seen in the

pre-transitional disks of RY Tau and WW Cha due to complications introduced by mispointing and insufficient data. However, these disks exhibit seesaw-like variability (Figures 11 and 12). Taking the modeling described above into consideration, one can surmise that the variability in these disks is also due to an inner wall which varies in height. While the variations in the SED for many objects in the sample can be reproduced by changes in the height of the inner wall, we note that other explanations that have not been considered here may possibly result in similar SED behaviors. We leave exploration of this to future work.

5.1.2. Optically Thin Dust Region

In the pre-transitional disks of IP Tau and T56 the 10 μm silicate emission changes (Figure 15). This feature is dominated by sub-micron sized grains in the optically thin dust region located within the disk gap. We can reproduce the change in this emission by adjusting the amount of small dust in this region. Alternatively, given that the spatial distribution of this dust is largely unknown, it is possible that part of the optically thin dust region is in the shadow of the inner wall and so in some cases the amount of dust we see in this region varies as the height of the inner wall changes. In LkCa 15 and SZ Cha, the 10 μm silicate emission does not change. This indicates that the optically thin dust is vertically distributed in such a way that it is not shadowed by the inner wall. This could suggest that there is more dust in the gap that we do not detect. Therefore, the values for the amount of dust in the gaps of pre-transitional disks should be taken as a lower limit. Alternatively, this optically thin dust could be heated indirectly. In order to explain the presence of the 10 μm silicate emission feature in self-shadowed Herbig Ae/Be stars, Dullemond & Dominik (2004) proposed that light reaches the shadowed regions after being scattered off of the upper parts of the inner wall. In addition, they suggest that the thermal emission from the wall may also irradiate the shadowed region. Similar mechanisms may be at work in the optically thin regions of pre-transitional disks.

Of the four transitional disks in the sample, two exhibit variability: CS Cha and GM Aur (Figure 16). In CS Cha, only the 10 μm silicate emission changes between epochs. We can explain this by varying the amount of optically thin dust located within the central cavity. On the other hand, the dust in CS Cha could be spatially distributed in such a way as to cause the observed variability. For example, CS Cha is a spectroscopic binary and, while we do not see the type of variability expected for a circumbinary disk (Nagel et al. 2010), the optically thin dust in the hole of CS Cha could be unevenly distributed in such a way that the alignment of the binary system at the time when the GO data was taken illuminates more of the dust. High-resolution near-infrared interferometry of this object would be ideal to test this.

To fit the variability of GM Aur, we not only change the amount of optically thin dust in the hole, we have to change the height of the outer wall as well. Espaillat et al. (2010) demonstrated that GM Aur’s near-infrared excess continuum between 1–5 μm could be reproduced by emission from sub-micron-sized optically thin dust. These variability data suggest that there

is some optically thick structure in the inner disk perhaps composed of large grains and/or limited in spatial extent which does not contribute substantially to the emission between 1–5 μm and leads to shadowing of the outer disk. Alternatively, it could be that while the dust in the hole is vertically optically thin, it becomes horizontally optically thick at some radius and shadows the outer disk (Mulders et al. 2010). This scenario implies that the vertical extent of the optically thin dust region changes to produce a shadow commensurate with the variable emission at the longer wavelengths. Then again, the fact that we have to change the height of the outer wall of GM Aur to fit its variability may not be linked to shadowing of the outer wall by inner disk material, but by changes in the outer wall itself. For example, our models assume the outer wall is axisymmetric, but changes in the visible area of the wall could lead to different emission from the outer wall. We note however that the orbital timescales at the outer wall are much longer than the timescales probed in this work. The case of GM Aur needs to be explored further.

5.1.3. The Unique Case of CR Cha

CR Cha displays a considerable change in slope at 6 μm (Figure 14). In the other objects in this sample, the emission at this wavelength is typically dominated by either an optically thick inner wall or an optically thin dust region. This could suggest that the inner disk alternates from being dominated by optically thick material in the GTO epoch to being dominated by optically thin dust at the time that the GO observations were taken 3 yrs later. Alternatively, the change in slope at 6 μm could also be due to a substantial decrease in the temperature of the inner wall. Accordingly, we reproduced the variability observed in CR Cha by fitting it with a pre-transitional disk model in the GTO epoch and both a transitional and pre-transitional disk model in the GO epoch.

In the case where we fit the GO spectra with a transitional disk model, it follows that once the optically thick inner wall disappears, we see all of the optically thin dust within the disk hole. Hence there is substantially more 10 μm emission in the GO observations which we reproduce by increasing the amount of dust in the optically thin region. We note that the height of the outer wall in the GO epoch, where we assume that there is no shadowing, is less than the height of the wall in the GTO epoch when there is an optically thick inner wall shadowing part of the outer wall. Given that we take the shadowed portion of the outer wall into account in the case where the inner disk is optically thick, this decrease in wall height in the case where the inner disk is optically thin may imply that a portion of the outer wall is still shadowed. As in the case of GM Aur discussed in § 5.1.2, this suggests that either there is an optically thick structure in the inner disk that we cannot detect or that the vertically optically thin dust is radially optically thick. It is expected that the optically thick inner disk in pre-transitional disks will disappear at some point via accretion onto the star and/or a lack of resupply of dust and gas from the outer disk, leaving behind a transitional disk. However, the viscous timescale at these radii is on the order of 10^4 yrs making it improbable that we are detecting this transition.

Alternatively, in the case where we fit the GO spectra

with a pre-transitional disk model, we have to decrease the temperature of the wall from 1400 K (in the GTO fit) to 800 K. This corresponds to a change in radius from 0.2 AU to 1 AU. This may not be a viable model, since it is not clear what process could make the dust grains sublime above 800 K. In any event, the amount of optically thin dust in the gap remains about the same as seen in the GTO epoch.

Near-IR spectra at shorter wavelengths are necessary to decipher whether or not the inner disk of CR Cha is optically thick or optically thin. Multi-epoch spectra would be useful in constraining if the nature of the inner disk changes with time. Millimeter confirmation of the hole in CR Cha with *ALMA* is necessary to decipher if there is indeed a cavity in this disk.

5.2. Physical Mechanisms Behind Variable Disk Structures

5.2.1. Variable Accretion

A higher mass accretion rate will lead to a higher surface density in the disk and so the height of the wall (defined as the point where the optical depth to the stellar radiation reaches ~ 1) will increase (Muzerolle et al. 2004). In the cases of LkCa 15, SZ Cha, UX Tau A, IP Tau, T56, and T35 the change in the near-IR emission could be explained if the mass accretion rate varies by factors of ~ 3 –10 relative to the mass accretion rate used in this work. Studies have shown that mass accretion rates onto the star are indeed variable. In the transitional disk of TW Hya, accretion rates of $5 \times 10^{-10} \text{ M}_{\odot} \text{ yr}^{-1}$ (Muzerolle et al. 2000), $2 \times 10^{-9} \text{ M}_{\odot} \text{ yr}^{-1}$ (Herczeg et al. 2004), and $3.5 \times 10^{-9} \text{ M}_{\odot} \text{ yr}^{-1}$ (Ingleby & Calvet, submitted) have been measured. Alencar & Batalha (2002) found that TW Hya’s mass accretion rate varied between $10^{-9} - 10^{-8} \text{ M}_{\odot} \text{ yr}^{-1}$ over a one year period and that smaller variations were seen even on periods of days. While these accretion rates have been measured onto the star (i.e. the accretion columns), the orbital timescales at the dust sublimation radius (~ 1 week) are within the timescales of infrared variability seen. Hence the changes in the mass accretion rate in the inner disk necessary to change the wall height are plausible.

However, if the mass accretion rate increases, the radius of the dust sublimation radius will increase as well given that $R_{\text{wall}} \propto (L_{*} + L_{\text{acc}})^{0.5}$ and $L_{\text{acc}} \sim GM_{*}\dot{M}/R_{*}$ (D’Alessio et al. 2005). The change in the radius is much larger than the change in the wall height. For a wall with a relatively similar height and a larger radius, the shadow on the outer wall (see Equations A4 and A5 in the appendix of Espaillat et al. 2010) will not be large enough to diminish the flux at the longer wavelengths to the levels observed. Therefore, a change in mass accretion rate alone cannot explain the observed SEDs in the pre-transitional disks in our sample, indicating that the variability in these disks is due to a change in the wall height while keeping the radius of the wall fixed.

Earlier we noted that to fit the variability in the transitional disks of GM Aur and CS Cha and the pre-transitional disks of IP Tau and T56, we altered the amount of dust in the optically thin region. It has been proposed that this small dust exists in the holes of some objects due to dust traveling with gas from the outer disk and into the inner disk after being filtered at the outer

wall (Rice et al. 2006). In this scenario, changes in the amount of dust in the optically thin region could be due to variable mass accretion rates.

The reason behind the variability of accretion is not understood. Turner et al. (2010) proposed that changes in the disk magnetic flux coupled with changes in the X-ray luminosity can lead to substantial changes in the mass accretion rates of typical TTS disks. However, this applies to accretion flows onto the star. For the inner disk, accretion variability could be linked to the formation mechanism behind cavities in disks, namely planets. One can speculate that changes in mass accretion rate could be due to planetary companions which alter the accretion flow in the inner disk regions, eventually getting onto the star. Lubow & D’Angelo (2006) and Zhu et al. (2010) demonstrate that planets will affect the mass accretion rate into the inner disk. It is possible that this could occur on the timescales seen here given that the 1–3 yr variability observed in our sample corresponds to orbital timescales of 1–2 AU, plausible radii for planets to be located.

5.2.2. *Disk Warps*

The changes seen in the inner disk could be due to warps. To explain the variability seen in the transitional disk of LRL 13, Muzerolle et al. (2009) proposed that the variability was due to dynamical changes in the inner disk, particularly in the form of disk warps. Flaherty & Muzerolle (2010) showed that the seesaw-like variability observed could be explained by models of a disk with an inner warp which leads the height of the inner disk to change with time. Such warps could be due to the presence of multiple planets in the disk. While a disk would damp the eccentricity of a single planet, multiple planets would be able to maintain eccentric orbits which would induce modulations that would effect the inner disk edge (D’Angelo et al. 2006), leading to the change in the height of the inner wall needed to reproduce the observations of pre-transitional disks.

Warps caused by planets could account for the timescales of the flux changes seen in our sample. Variability on timescales of 1–3 yr corresponds to orbital timescales of 1–2 AU and 1 wk timescales correspond to 0.07 AU. Radii of 1–2 AU are plausible locations for planetary companions. A radius of 0.07 AU is comparable to the dust destruction radius. Many “hot Jupiters” are known to exist at radii < 0.1 AU (Marcy et al. 2005), comparable to or within the magnetospheric radius of their host stars and well within the dust sublimation radius, most likely reaching their current positions via migration (Rice et al. 2008).

5.3. *The Composition of Silicate Dust in the Disk*

The formation of crystalline silicates requires high temperatures (Fabian et al. 2001). One proposed mechanism for the formation of crystalline silicates is accretion heating in the innermost disk, close to the dust sublimation radius (e.g. Gail 2001). However, in our objects crystalline silicates can be seen in the outer wall, which is located at radii much further than the dust sublimation radius. In several other studies, it is also found that crystalline silicates are in the outer regions of the disk (Bouwman et al. 2008; Watson et al. 2009; Sargent et al.

2009; Olofsson et al. 2009, 2010). This suggests that large-scale radial mixing is necessary to transport the crystalline silicates that form near the dust destruction radius out to larger radii in the disk (e.g. Boss 2004; Gail 2004; Keller & Gail 2004; Ciesla 2007), but this must occur before the hole or gap forms. Alternatively, crystalline silicates can form in the inner disk due to heating from shocks in the disk created by planets (Desch et al. 2005; Boss & Durisen 2005; Bouwman et al. 2008). In this case, the crystalline silicates would still need to be transported to the outer disk. Changes in the accretion rate or stellar luminosity could possibly lead to the formation of crystalline silicates in the surface layers of the disk as proposed in the case of EX Lupi (Ábrahám et al. 2009). Or as noted by Espaillat et al. (2007a), local processing may be due to collisions of larger bodies that produce small grains heated to temperatures high enough to create crystals.

One interesting by-product of this study is the possibility to explore how or if the silicate composition is linked to the variability seen in the sample. Indeed, we find that the four disks with 1 wk variability contain the highest amounts of crystalline silicates in the sample. In UX Tau A, ISO 52, T35, and T56, the outer wall is composed of $\sim 19\%$, 20% , 60% , and 18% crystalline silicates, respectively. (The next highest fraction is $\sim 13\%$, found in SZ Cha.) The optically thin regions of ISO 52 and T56 are $\sim 20\%$ and $\sim 25\%$ crystalline silicates, respectively, higher than any other disks in the sample by a factor of at least 2. In larger studies of samples focusing on low-mass stars, there is very little correlation between the crystalline silicate mass fraction and any stellar or disk property aside from the positive correlations with other crystalline silicate abundances and the amount of dust settling in the disk (Sargent et al. 2009; Watson et al. 2009).

The trend between crystalline mass fraction and short timescale variability points to a link behind the underlying cause of the silicate composition of the disk and the seesaw behavior observed. We propose that this link is planets. Planets can instigate warps, shocks, and collisions in the disk which can lead to both changes in the height of the inner disk wall and a higher abundance of crystalline silicates. Planets can also lead to recurring changes in the disk. In T56 and T35, the variability observed at $\lambda > 20 \mu\text{m}$ appears to oscillate between a maximum and minimum flux. For T56, the flux at these wavelengths is at a minimum in the GTO epoch, it increases in the GO1 epoch, and in the GO2 epoch it decreases back to the same flux observed in the GTO epoch. In T35, the GTO and GO1 spectra are both at the maximum and the GO2 spectrum is lower. Such changes point to a periodic origin, such as a planetary orbit. Since planets are likely present in most of the disks in this sample, it would seem that these four disks with high amounts of crystalline silicates either have more planets or that the presence of hot Jupiters (see § 5.2.2) is significant.

6. SUMMARY & CONCLUSIONS

In this work we see various types of variability on 3–4 year timescales and in some cases we see variability on 1 week timescales. The dominant type of variability observed can be classified as seesaw-like behavior, whereby the emission at shorter wavelengths varies inversely with

the emission at longer wavelengths.

We attempted to understand the origin of the variability in pre-transitional and transitional disks by modeling the overall SEDs at different epochs. For many of the pre-transitional disks we find that the variability can be explained by changing the height of the inner disk wall and hence the shadow on the outer disk. Typically, the height of the wall varies by $\sim 20\%$. We also perform SED model fitting for the transitional disks GM Aur and CS Cha. To fit the variability of GM Aur, we vary the amount of optically thin dust in the hole and the height of the outer wall. In CS Cha, only the $10\ \mu\text{m}$ silicate emission changes between epochs and so we only alter the amount of dust in the optically thin region. The transitional disks DM Tau and T25 are the only two disks in the sample which display no variability. These disks' inner regions do not contain discernible amounts of dust.

We propose that planets are responsible for the changes observed in our sample. Overall, it seems that most of the variability seen is due to material in the inner disk casting a shadow on the outer disk. The height of the inner wall can vary due to disk warps caused by planets in the disk. We can also link the silicate dust compositions found in this work to the presence of planets. We find that crystalline silicates are common in the outer disks of our objects, too far from the central star to be

explained by most crystallization mechanisms. In addition, the four disks in our sample which have the highest crystalline silicate mass fractions vary on 1 wk timescales. In two of these four disks, we see periodic changes in the infrared emission. Planets can cause shocks and collisions which can heat the dust to high enough temperatures to crystallize the dust. Planets can also lead to short timescale and periodic variability. Follow-up variability studies conducted with the *James Webb Space Telescope* will give us the simultaneous, multi-wavelength data needed to test if the variability observed in our sample is periodic as well as the sensitivity to significantly expand the sample size.

We thank the referee for a constructive and thorough report. We thank Lee Hartmann for providing comments on the manuscript and Steve Lubow for useful discussions. C. E. was supported by the National Science Foundation under Award No. 0901947. E.F. was supported by NASA through the Spitzer Space Telescope Fellowship Program, through a contract issued by JPL/Caltech under a contract with NASA. P. D. acknowledges a grant from PAPIIT-DGAPA UNAM. E. N. acknowledges a postdoctoral grant from CONACyT. N. C. acknowledges support from NASA Origins Grant NNX08AH94G.

APPENDIX

(Objects here are organized in the order in which they appear in Figures 10 through 17.)

LkCa 15

LkCa 15 is a pre-transitional disk in the Taurus cloud, previously identified and modeled in detail by Espaillat et al. (2007a, 2010). The large cleared region in this disk has been confirmed with millimeter imaging (Andrews et al, in prep; Piétu et al. 2006). Here we take the model presented in previous works and modify it to better fit the silicate dust features in the SED and fit the observed variability. Figure 10 (top left) shows the three *Spitzer* IRS spectra assembled for this study. The GO1 and GO2 spectra agree with one another. The GTO spectrum is higher than the GO spectra at $\lambda < 8\ \mu\text{m}$ and lower at $\lambda > 15\ \mu\text{m}$. The $10\ \mu\text{m}$ silicate emission remains the same in all three spectra. Two additional spectra of LkCa 15 were taken two days apart in November 2008 by GO Program 40338 (Nov 5; PI: Najita) using the SH module ($10\text{--}19\ \mu\text{m}$) and GTO Program 50498 (Nov 7; PI: Houck) using the LH module ($19\text{--}37\ \mu\text{m}$). We find that the SH data agree with our GTO and GO data at $\lambda < 15\ \mu\text{m}$ and our GO data at $15\text{--}19\ \mu\text{m}$; the LH data agree with our GTO data. This could suggest that the type of variability seen in LkCa 15 occurs on timescales as short as 2 days. However, this is speculative and simultaneous data at shorter and longer wavelengths would be needed to test this.

Before trying to explain the variability, we first modeled the GTO spectrum in detail in order to better fit the silicate dust features. The composition of the silicate dust in the outer wall and disk that gave the best fit to the IRS spectrum is listed in Table 4. The size of the gap is 39 AU. We note that to better fit the upward slope of the IRS spectrum beyond $\sim 30\ \mu\text{m}$ we used an ice abundance of 0.0012. The abundance of troilite and organics given in § 4.2.3 was not changed. As stated in § 4.2.3, the inner wall is made up of olivine silicates. The optically thin dust region spans 15 AU in the disk and contains ISM-sized dust (i.e. $a_{\text{min}}=0.005\ \mu\text{m}$ and $a_{\text{max}}=0.25\ \mu\text{m}$; Mathis et al. 1977). Within 1 AU the dust is 32% organics, 13% troilite, and 55% silicates. Between 1–15 AU the dust is made up of 12% organics, 9% troilite, and 79% silicates. The compositions of the silicates in these regions are listed in Table 5. We found that having both olivines and pyroxenes was necessary to fit the SED. The olivines in the inner 1 AU contribute mostly to the $10\ \mu\text{m}$ silicate emission. If olivines were located further than 1 AU in the optically thin region, they would produce too much $20\ \mu\text{m}$ silicate emission. Therefore, we used pyroxenes in the outer radii of the optically thin region to fit the $20\ \mu\text{m}$ silicate emission feature. The optically thin dust region contains $2 \times 10^{-9}\ M_{\odot}$ of small dust.

We can fit the variability observed by changing the height of the inner wall (Figure 10, top left; GTO fit: solid line; GO1/GO2 fit: broken line). In the GTO spectrum, the inner wall height is 0.009 AU and for the GO spectra it is 0.007 AU, corresponding to a 22% decrease in the height of the wall. The small change in the inner wall is enough to cause the difference in flux observed at the longer wavelengths. When the inner wall is higher (in the GTO case), there is a larger shadow on the outer wall and hence the emission seen from the outer wall is less and the IRS spectrum is lower than the GO spectra. In the GO case, the inner wall is lower and so the shadow on the outer wall is smaller. Therefore, we see more emission and the flux of the GO spectra longwards of $20\ \mu\text{m}$ is higher. The $10\ \mu\text{m}$ silicate emission does not change. This emission is dominated by the small dust in the optically thin region.

In the top right panel of Figure 10 we present the best fit model to the GTO IRS spectrum and the broad-band SED.

The disk properties of LkCa 15 are listed in Table 3. The inner wall has a temperature of 1400 K and has a maximum grain size of $1\ \mu\text{m}$ following the best-fit found by fitting near-IR spectra from $1\text{--}5\ \mu\text{m}$ by Espaillat et al. (2010). The inner wall is located at a radius of 0.15 AU. The height of the inner wall varies as outlined above. The outer wall has a temperature of 110 K, corresponding to a radius of 39 AU. The height of the outer wall is about 5 AU. The outer disk has $\alpha=0.0005$, $\epsilon=0.001$, and a mass of $0.1\ M_{\odot}$. The differences between the parameters presented here and those of Espaillat et al. (2010), especially the ~ 20 AU difference in radius, are due to the different dust composition adopted. See the discussion in that work for details on how different dust compositions lead to differing fits and hence derived disk properties.

We note that a pre-transitional disk structure for LkCa 15 has also been independently found through SED modeling by Mulders et al. (2010). However, those authors assume the star is a point source and so the shadowing of the outer disk is not properly calculated. Espaillat et al. (2010) and this work take into account that the star is a finite source and the ensuing effect on the heating of the outer disk.

SZ Cha

SZ Cha was first identified as a pre-transitional disk candidate by Kim et al. (2009). Here we present the first detailed model of this object. The GO1 and GO2 IRS spectra of SZ Cha agree with one another (Figure 10, middle left). However, the GO spectra are higher than the GTO spectra at $\lambda < 8\ \mu\text{m}$ and lower at $\lambda > 15\ \mu\text{m}$. The $10\ \mu\text{m}$ silicate emission is similar in all three spectra.

One additional SH spectra of SZ Cha was taken in GO Program 40247 (PI: Calvet) on August 17, 2008. We find that this spectrum agrees with our GTO and GO spectra between $10\text{--}13\ \mu\text{m}$. However, between $13\text{--}19\ \mu\text{m}$ the flux in the SH spectrum is lower than both the GTO and GO observations. In particular, the flux is about 15% lower in the SH observations than our GO observations. We do not have simultaneous data at shorter wavelengths and so we do not model the SH data here. However, these SH observations support that the $10\ \mu\text{m}$ silicate emission feature does not vary while the emission at longer wavelengths does. Furthermore, the SH data were taken two months after our GO observations, showing that variability in SZ Cha occurs on shorter timescales than the 3 year timescale probed by our GTO and GO observations.

We fit the IRS spectrum with a 18 AU gap and the silicate dust mixture listed in Table 4. The optically thin dust extends up to 1 AU in the disk and contains $0.005\text{--}3\ \mu\text{m}$ dust composed of 12% organics, 9% troilite, and 79% silicates. The silicate composition can be found in Table 5. The gap contains $2 \times 10^{-12}\ M_{\odot}$ of small optically thin dust.

We fit the observed variability by adjusting the height of the inner optically thick disk's wall (Figure 10, middle left; GTO fit: solid line; GO1/GO2 fit: broken line). In the GTO spectrum, the inner wall height is 0.006 AU and for the GO spectra it increases by 33% to 0.008 AU. This change in the inner wall is enough to cause the difference of flux observed at the longer wavelengths. The $10\ \mu\text{m}$ silicate emission, which is dominated by the small dust in the optically thin region, does not change significantly. In the middle right panel of Figure 10 we present the best fit model to the GTO IRS spectrum and the broad-band SED. Model parameters are listed in Table 3.

UX Tau A

UX Tau A was previously identified as a pre-transitional disk and modeled by Espaillat et al. (2007a, 2010). Millimeter imaging has confirmed that there is a large cavity in this object (Andrews et al, in prep). As in the case of LkCa 15, we re-model UX Tau A, paying particular attention to fitting its silicate emission features in order to better reproduce the variability.

The variability seen in UX Tau A is similar in some respects to that seen in LkCa 15, but very different in others. The GO spectra display variability like that of LkCa 15, but without the presence of a discernible $10\ \mu\text{m}$ silicate emission feature (Figure 10, bottom left). Shortwards of $\sim 18\ \mu\text{m}$, the GO1 spectrum (green) is higher than the GO2 spectrum (blue). At longer wavelengths the behavior switches, with the GO2 spectrum now higher than the GO1 spectrum.

The GTO spectrum of UX Tau A is higher than both of the GO spectra at all wavelengths (Figure 10, bottom left). The overall decrease in the emission between our GTO and GO spectra suggests that the luminosity at the bands at which the disk absorbs stellar radiation has decreased between the two epochs. Without simultaneous optical data, we cannot test this. Alternatively, the mass accretion rate of the disk could have decreased over time. Two LH spectra were taken by GO Program 2300 (PI: Carr) on March 14, 2005 and GTO Program 50498 (PI: Houck) on November 6, 2008. Both are consistent within the observational uncertainties with our GTO spectrum which was taken in February 2004. However, we do not have data at $< 19\ \mu\text{m}$ and cannot discern how/if the SED changes at shorter wavelengths.

One SH spectrum and one LH spectrum was taken in GO Program 30300 (PI: Najita) on March 22, 2007, between the times at which our GTO observations and GO observations were taken. The SH spectrum agrees with our GO2 spectrum between 10 and $13\ \mu\text{m}$, but is substantially lower at longer wavelengths (Figure 18). The LH spectrum is also lower than our GTO and GO data. This suggests that at $\lambda > 13\ \mu\text{m}$ UX Tau A returns to the higher fluxes seen in our GTO and GO data periodically, possibly within about two years. Again, we would need simultaneous data at $\lambda < 10\ \mu\text{m}$ to come to a firmer conclusion.

We note that UX Tau A has one companion at $2.5''$ (UX Tau C) and one at $5.6''$ (UX Tau B). In November 2002, UX Tau B was fainter than A by a factor of 12 at $11.8\ \mu\text{m}$, while UX Tau C was fainter than A by a factor of 60 (McCabe et al. 2006). UX Tau B and C entered all the IRS slits except in the case of the SL slit where UX Tau B did not enter the slit. UX Tau B and C do not have a near-infrared excess and are not accreting (White & Ghez 2001) and so we can conclude that they most likely do not have disks. Therefore, they would not contribute at wavelengths

$>13\mu\text{m}$ where we see a large change in flux in Figure 18. Therefore, this variability is probably not due to large changes in the fluxes of these companions.

In Table 4 we list the silicate dust composition that best explains the crystalline silicate features seen in the IRS spectrum beyond $20\mu\text{m}$. To better reproduce the spectrum at longer wavelengths we removed ice from the outer wall and disk. Our model of UX Tau A includes no optically thin dust within the gap, which is 30 AU in radius.

As in the case of LkCa 15, we can fit the variability observed between the GO spectra by varying the height of the inner wall (Figure 10, bottom left; GO1 fit: solid line; GO2 fit: broken line). In the GO1 spectrum the height of the wall is 0.006 AU and it decreases by 17% to 0.005 AU in the GO2 spectrum. This difference in the inner wall height (and hence the amount of shadowing on the outer disk wall) is enough to cause the observed flux change at the longer wavelengths. Here we adopt the temperature for the inner wall found by Espaillat et al. (2010, 1550 K) based on fitting near-IR spectra. However, we find that we can fit the SHLH spectrum (Figure 18) with an inner wall temperature of 1800 K (corresponding to a radius of 0.1 AU) and a height of 0.0053 AU. Moving the wall closer to the star produces a larger shadow on the outer wall, and reproduces the SHLH spectrum well. However, we do not have simultaneous data at shorter wavelengths and hence cannot test if this wall fits the SED at $\lambda < 10\mu\text{m}$ at the time the SHLH spectrum was taken. Further observations are needed to test if the temperature of the inner wall of UX Tau A varies with time.

The bottom right panel of Figure 10 has the best fit model to the GO1 IRS spectrum and the broad-band SED. Relevant disk properties are listed in Table 3. The differences between the parameters presented here and those of Espaillat et al. (2010) are substantial, particularly the 40 AU difference in the radius of the gap. Again, this is due to the different dust composition adopted. Including crystalline silicates (forsterite, enstatite, silica) has a substantial effect on the opacities and hence disk properties.

RY Tau

Analysis by Furlan et al. (2009) identified RY Tau as an outlier with respect to its $\text{EW}(10\mu\text{m})$. RY Tau had much more silicate emission than could be explained by the full disk model grid used in that study. As a part of this variability study, we attempted to fit the disk of RY Tau with a full disk model and were unsuccessful. It is not possible to simultaneously fit the existing millimeter and IRS data, even within the uncertainties of the observations. The strong $10\mu\text{m}$ silicate emission cannot be reproduced by a typical full disk model and could be a sign that RY Tau is a pre-transitional disk with a small gap that contains some small optically thin dust, as suggested by Espaillat (2009) and Furlan et al. (2009). Submillimeter imaging by Isella et al. (2010) supports that there is an inner cavity in this disk.

Figure 11 (left) shows the three *Spitzer* IRS spectra assembled for this study. The GO spectra agree with one another. The GTO observation was mispointed, and so we cannot confidently constrain the amount of variability between the GTO and GO spectra nor the pivot wavelength. In addition, the $10\mu\text{m}$ region in the GO spectra were saturated and we cannot reliably fit the emission from the inner disk of RY Tau. Two additional high-resolution spectra of RY Tau were taken in GO Program 40113 (SH; PI: Lahuis) and Program 50641 (LH; PI: Carr), both on October 2, 2008. We find that the SH spectrum agrees with our GO spectra shortwards of $15\mu\text{m}$. However, at longer wavelengths the flux is consistent with both the GTO and GO observations within the observational uncertainties. The LH spectrum is also consistent with both the GTO and GO observations.

We found that we could fit the GTO IRS spectrum with an 18 AU gap (Figure 11, both panels) and a silicate dust mixture in the outer wall and disk consisting of predominantly olivine silicates (Table 4). The optically thin dust in the gap extends up to 1 AU in the disk and contains $3 \times 10^{-10} M_{\odot}$ of $0.005\text{--}3\mu\text{m}$ dust composed of 19% organics, 15% troilite, and 66% silicates. The silicates in the optically thin dust region have the same composition as that in the wall and outer disk (Table 5). Disk properties are listed in Table 3. Here we adopt the same mass accretion rate as Calvet et al. (2004, Table 2).

WW Cha

WW Cha displays the same type of variability as seen in LkCa 15, SZ Cha, and UX Tau A (Figure 12). The GO1 and GO2 IRS spectra of WW Cha agree with one another and the GO spectra are higher than the GTO spectra at $\lambda < 8\mu\text{m}$ and lower at $\lambda > 15\mu\text{m}$. However, because the GO observations were mispointed, we cannot confidently constrain the amount of variability nor the pivot wavelength. Clearly there is true variability as we would have expected the spectra to have lost flux overall due to the mispointing, but at the shorter wavelengths the GO spectra are higher than the GTO spectra. We note that there are no additional *Spitzer* IRS spectra of WW Cha available in the archive.

We do not model this object because it was mispointed in the GO observations and we do not have a reliable mass accretion rate estimate. Based on the SED it appears that the optical photometry is unreliable. On the other hand, it could be that the accretion rate of WW Cha is very high, which would lead to a substantial excess above the stellar photosphere $< 1\mu\text{m}$. If the photometry is accurate, we derive a mass accretion rate of $8 \times 10^{-7} M_{\odot} \text{ yr}^{-1}$, making WW Cha a high accretor like DR Tau. D'Alessio et al. (in prep) discuss the considerations that must be taken into account when modeling high accretors. Because of these reasons and the fact that the GO spectra were mispointed, we do not attempt to model WW Cha in this work. However, the GTO IRS spectrum of WW Cha is similar in morphology to that of LkCa 15, suggesting that it is a pre-transitional disk as well.

ISO 52

ISO 52 is located in Chamaeleon and its SED is presented in Figure 13. ISO 52 displays seesaw-like behavior; however, it is very different from any of the other disks in the sample. The GO spectra (which agree with one another) are substantially higher than the GTO spectra at $\lambda < 9 \mu\text{m}$ and lower at $\lambda > 12 \mu\text{m}$. The $10 \mu\text{m}$ silicate emission feature almost disappears in the GO spectra due to the increasing continuum in the $5\text{--}8 \mu\text{m}$ region. There are no additional *Spitzer* IRS spectra of ISO 52 available in the archive.

As in the case of WW Cha, we do not have a mass accretion rate estimate for ISO 52; there is no U-band photometry for this object. However, for the purposes of reproducing the observed variability we modeled the SED assuming a mass accretion rate of $1 \times 10^{-8} \text{ M}_{\odot} \text{ yr}^{-1}$. We fit the IRS spectrum with a 10 AU gap and the silicate dust mixture listed in Table 4. The optically thin dust extends up to 1 AU in the disk and contains $2 \times 10^{-12} \text{ M}_{\odot}$ of $0.005\text{--}5 \mu\text{m}$ dust composed of 42% organics, 11% troilite, and 47% silicates (Table 5).

We fit the observed variability by adjusting the height of the inner optically thick disk's wall (Figure 13, left; GTO fit: solid line; GO1/GO2 fit: broken line). In the GTO spectrum, the inner wall height is 0.0006 AU and for the GO spectra it is 0.003 AU. This corresponds to an increase of 400% in the wall height, the largest change by far in any of the objects in the sample. To fit the GO observations, the optically thin dust region has to be extended to 2 AU and contains three times more dust to account for the emission at $20 \mu\text{m}$ since the contribution from the outer wall at these wavelengths is significantly less relative to its contribution in the GTO epoch.

In the right panel of Figure 13 we present the best fit model to the GTO IRS spectrum and the broad-band SED. We stress that the mass accretion rate of ISO 52 is not known. As such we do not list its disk model parameters in Table 3 along with disks where the mass accretion rate is known and hence the disk parameters are better constrained. Here we briefly summarize the disk parameters obtained by adopting a mass accretion rate of $1 \times 10^{-8} \text{ M}_{\odot} \text{ yr}^{-1}$. The inner wall is located at a temperature of 1400 K with a radius of 0.05 AU. It has a maximum grain size of $10 \mu\text{m}$ and its height varies as outlined above. The outer wall has a temperature of 130 K, corresponding to a radius of 10 AU. The height of the outer wall is about 1 AU. There is no millimeter information for this object and so we do not model the outer disk.

CR Cha

Analysis by Furlan et al. (2009) identified CR Cha as an outlier with respect to its $\text{EW}(10 \mu\text{m})$. Here we find that it is not possible to simultaneously fit the existing data with a full disk model, as in the case of RY Tau. Figure 14 (left) shows the three *Spitzer* IRS spectra assembled for this study. The GO1 and GO2 spectra agree with one another and are both higher than the GTO spectra at $\lambda > 6 \mu\text{m}$ and lower at $\lambda < 6 \mu\text{m}$. We note that there are no additional *Spitzer* IRS spectra of CR Cha available in the archive.

From the substantial change in slope at $\sim 6 \mu\text{m}$, one could infer that there is either a change in the nature of the emission from optically thick to optically thin or a substantial change in the temperature of the inner wall. We found that we could fit the GTO data with a pre-transitional disk model and the GO data with both a transitional and pre-transitional disk model. In all models the outer wall is located at 10 AU and is composed of the silicate mixture listed in Table 4. We note that attempts to fit the variability of the SED with changes in the mass accretion rate were unsuccessful. High-resolution near-interferometric data of this object is necessary to constrain how or if the inner disk structure responsible for the near-IR variability changes with time.

In the GTO fit (Figure 14, left, solid line), there is an inner wall with a temperature of 1400 K, a radius of 0.26 AU, and a height of 0.008 AU. The outer wall has a height of 0.8 AU. The optically thin dust in the gap extends up to 1.5 AU and contains $1.8 \times 10^{-11} \text{ M}_{\odot}$ of $0.005\text{--}10 \mu\text{m}$ dust composed of 12% organics, 10% troilite, and 78% silicates. The silicates in this region have the same composition as that in the outer wall and disk (Table 5).

In the GO pre-transitional disk model fit (Figure 14, left, dotted line), the inner wall has a temperature of 800 K, corresponding to a radius of 1 AU, and a height of 0.03 AU. The outer wall has a height of 0.8 AU. The optically thin region spans 1–1.5 AU, and contains $1.3 \times 10^{-11} \text{ M}_{\odot}$ of $0.005\text{--}10 \mu\text{m}$ dust composed of 8% organics, 6% troilite, and 86% silicates.

In the GO transitional disk model fit (Figure 14, left, dashed line), there is no inner wall. The optically thin region spans the same radii as in the GTO fit, but the amount of dust has increased by a factor of two and is now composed of 17% organics, 13% troilite, and 70% silicates. The outer wall is also the same as that in the GTO fit, except that the height of the outer wall differs. In the GTO fit, which takes into account shadowing by the inner wall, the height of the outer wall is 0.8 AU and in the GO fit, where there is no shadowing it is 0.5 AU high. This could imply that some portion of the outer wall is shadowed in the GO fit, where there is only optically thin dust in the inner disk.

The outer disk does not change between the epochs observed (Figure 14, right); properties are listed in Table 3.

IP Tau

Analysis by Furlan et al. (2009) identified IP Tau as an outlier with respect to $\text{EW}(10 \mu\text{m})$, as in the case of RY Tau. As a part of this work, we attempted to fit the disk of IP Tau with a full disk model and were unsuccessful. It is not possible to simultaneously fit the existing millimeter and IRS data, even within the uncertainties of the observations. Here we present the first detailed model of this object, assuming it is a pre-transitional disk. The GO1 and GO2 IRS spectra of IP Tau agree with one another within the uncertainties, but variability occurs between the GTO and GO spectra (Figure 15, top left). The variability seen in IP Tau differs from the variability discussed up to this point. The GTO spectra are higher than the GO spectra at $\lambda > 8 \mu\text{m}$. The seesaw-like behavior seen in LkCa 15, UX Tau A,

and SZ Cha is not conspicuous here. However, we attempt to reproduce the variability assuming that the inner wall varies within the observational uncertainties and are successful. We note that two additional IRS spectra of IP Tau were taken in GO Program 179 (PI: Evans) on February 8, 2005. We find that these SH and LH spectra are consistent with the GTO data in this paper (taken in February 2004) within the observational uncertainties.

The size of the gap in IP Tau is very small, about 2 AU wide. Details of the silicate dust mixture used in the outer wall and disk can be found in Table 4. The optically thin dust in the gap extends up to less than 0.5 AU and contains 0.005–4 μm dust composed of 17% organics, 13% troilite, and 70% silicates. The silicates have the same composition as that in the wall and outer disk. The gap contains $9 \times 10^{-13} M_{\odot}$ of small optically thin dust.

In Figure 5 there is no variability in IP Tau at the short wavelengths, at least not outside of the uncertainties of the observations. However, IP Tau displays variability at longer wavelengths similar to behavior observed in other objects in the sample that could be explained by varying the height of the inner wall. Therefore, we vary the height of the inner wall of IP Tau to fit the data within the uncertainties of the observations. For the GTO spectrum, the inner wall height is 0.006 AU and for the GO spectra it is 0.007 AU i.e. the height of the wall increases by 17% (Figure 15, top left; GTO fit: solid line; GO1/GO2 fit: broken line). This change in the inner wall reasonably reproduces the difference of flux at the longer wavelengths. The 10 μm silicate emission also decreases between the GTO and GO observations. This emission is dominated by the small dust in the optically thin region which may indicate that the amount of dust in this region is changing. We can reproduce the 10 μm emission in the GO spectra by reducing the amount of dust in the optically thin region by 20%. The contribution to the SED from the outer disk is shown in the top right panel of Figure 15. We list the disk's properties in Table 3.

T56

T56 is located in Chamaeleon and was first identified as a pre-transitional disk candidate by Kim et al. (2009). Here we present the first detailed model of this object. The spectrum of T56 is noisy at $\lambda < 8 \mu\text{m}$, but it seems to display the same type of pivot variability as seen previously between the GTO and GO1 spectra (Figure 5). The GO1 and GO2 spectra agree in their 10 μm silicate emission (Figure 7), which is lower than seen in the GTO spectrum. The GO2 and GTO IRS spectra of T56 agree with one another beyond 20 μm while the GO1 spectrum is higher at these wavelengths. There are no additional *Spitzer* IRS spectra of T56 available in the archive.

We fit the IRS spectrum with a 20 AU gap. The silicate dust mixture in the outer wall and disk is listed in Table 4. The optically thin dust region extends up to 1 AU in the gap and contains $1 \times 10^{-11} M_{\odot}$ of ISM-sized dust (in the GTO fit) composed of 23% organics, 14% troilite, and 63% silicates (see Table 5 for silicate composition).

As noted above, at $\lambda < 8 \mu\text{m}$ the SNR is poor and we cannot confidently tell if there is variability at these short wavelengths. However, we fit the observed variability by varying the height of the inner wall within the uncertainties of the observations, as we did in the case of IP Tau. In the GTO and GO2 spectra (Figure 15, middle left; GTO fit: solid line; GO2 fit: dotted line), the inner wall height is 0.002 AU and for the GO1 spectra (Figure 15, middle left; GO1 fit: dashed line) it is 0.001 AU, a 50% decrease. The 10 μm silicate emission, which is dominated by the small dust in the optically thin region, changes significantly and we reproduce this by decreasing the amount of optically thin dust by 19% between the GTO and GO observations.

In the middle right panel of Figure 15 we present the best fit model to the broad-band SED. Relevant disk properties are listed in Table 3. We note that the disk mass derived here is Toomre unstable, i.e. $Q < 1$ at about 100 AU. Given that we only have a single millimeter data point to constrain the outer disk, this mass is poorly constrained and more millimeter data is needed.

T35

T35 is located in Chamaeleon and was first identified as a pre-transitional disk candidate by Kim et al. (2009) and here we present the first detailed model of this object. T35 displays the same type of seesaw variability as seen in the previous objects. However, it more closely resembles UX Tau A, both in that it has no apparent 10 μm silicate emission and that it has strong crystalline silicate features. As in the case of T56, discerning the variability is complicated at the shorter wavelengths by poor SNR. At $\lambda < 10 \mu\text{m}$, we cannot confidently tell if there is variability at these short wavelengths. Interestingly, in the GO2 spectrum it seems that the slope changes at 7 μm . The GO1 and GTO IRS spectra of T35 agree with one another beyond 20 μm (Figure 15, bottom left). The GO2 spectrum is lower at these wavelengths. One additional SH IRS spectrum of T35 was taken in GO Program 40247 (PI: Calvet) on October 12, 2008. This SH spectrum is very noisy and consistent with all three spectra presented in this paper within the observational uncertainties.

We found that we could fit the IRS spectrum well with a gap of 15 AU and the silicate dust mixture listed in Table 4 (Figure 15, bottom left; GTO/GO1 fit: solid line; GO2 fit: broken line). As in the case of UX Tau A, there is no optically thin dust within the gap. At $\lambda < 10 \mu\text{m}$, the SNR is poor and we cannot confidently tell if there is variability at these short wavelengths. However, we fit the observed variability by varying the height of the inner wall within the uncertainties of the observations. In the GTO and GO1 spectra, the inner wall height is 0.005 AU and for the GO2 spectra it is 0.006 AU, a 20% increase in height, which leads to the difference of flux at the longer wavelengths. We cannot reproduce the change in slope seen in the GO2 spectrum at 7 μm . One can speculate that this is somehow related to the fact that in order to fit the SED we need a higher inner wall temperature (1800 K) than used in the other disks in this sample.

In the bottom right panel of Figure 15 we present the best fit model to the broad-band SED. Disk properties can be found in Table 3. We could only find a millimeter upper limit from Henning et al. (1993) which is not useful in

constraining the outer disk and so we do not include modeling of the outer disk. However, we can still reproduce the IRS emission beyond $20\ \mu\text{m}$ using only an outer wall. This reflects the point made in § 4.2 that the outer wall dominates the emission in this region of the IRS spectrum.

GM Aur

GM Aur was previously modeled in detail by Calvet et al. (2005). They found it had an inner disk hole of ~ 20 AU that contained some small optically thin dust grains. Veiling analysis of near-infrared spectra by Espaillat et al. (2010) confirmed that the inner disk of this object contained some optically thin dust and millimeter imaging by Hughes et al. (2009) confirmed the size of the hole. Here we take the model presented in these previous works and modify it to better fit the silicate dust features and the observed variability. Figure 16 (top left) shows the three *Spitzer* IRS spectra assembled for this study. The GO1 and GO2 spectra agree with one another. GM Aur displays seesaw-like behavior and a change in the strength of the $10\ \mu\text{m}$ silicate emission. However, the percentage change in the flux at shorter wavelengths is larger than that seen at the longer wavelengths beyond $20\ \mu\text{m}$.

Eight additional SL spectra of GM Aur were taken in GO Programs 20755 and 30896 (PI: Bary) in Oct 2005, March 2006, Oct 2006, and March 2007. We find no significant variability between these spectra and our GO spectra. We note that in many of the spectra the flux of the $10\ \mu\text{m}$ silicate feature is $\sim 3\text{--}5\%$ lower than in our GO observations and in AOR 19483648 the spectrum is lower at all wavelengths by $\sim 9\%$. However, these small flux changes are within the mispointing uncertainties discussed in § 3.3. The agreement between our GO spectra and the spectra in Programs 20755 and 30896 indicates that the change in GM Aur's emission occurred between the time the GTO observations were taken (27 February 2004) and the first epoch of Program 20755 (13 October 2005). Two high resolution spectra were taken in GO Program 30300 (PI: Najita) on March 14, 2007 using SH and LH. One additional LH spectrum was taken in GTO Program 50498 (PI: Houck) on November 10, 2008. The spectra from GO Program 30300 agree with our GO observations between 10 and $15\ \mu\text{m}$, but the observational uncertainties make it consistent with both our GO and GTO observations at longer wavelengths. The LH spectrum agrees with our GTO observations of GM Aur. We do not have simultaneous data at shorter wavelengths. However, assuming that the seesaw-like behavior of GM Aur holds, one can conjecture that the flux in GM Aur changed within one month between our GO observations (taken in October 2008) back to the flux observed in our GTO observations and the LH GTO observations. More observations with *JWST* would be needed to test this.

The silicate dust composition used in the outer wall and disk is listed in Table 4 (Figure 16, top left; GTO fit: solid line; GO1/GO2 fit: broken line). The hole is 23 AU in radius. The optically thin dust region extends up to 1 AU in the hole and contains $2 \times 10^{-12}\ M_{\odot}$ of $0.005\text{--}1\ \mu\text{m}$ dust composed of 32% organics, 12% troilite, and 56% silicates (see Table 5). We can reproduce the observed variability by decreasing the amount of dust in the optically thin region between the GTO and GO spectra by a factor of two. Assuming an outer wall that is not being shadowed, the outer wall changes in height from 2.9 AU in the GTO spectrum to 3.2 AU in the GO spectra. This could point to shadowing by the dust in the hole on the outer disk wall, possibly due to opaque structure in the dust within the hole. We do not include the shadowing of this region and leave that to future work. In the top right panel of Figure 16 we present the best fit model (Table 2) to the broad-band SED.

CS Cha

CS Cha was previously modeled by Espaillat et al. (2007b). It has been identified as a spectroscopic binary (Guenther et al. 2007), but here we use a circumstellar disk model for simplicity. Figure 16 (second, left) shows the three *Spitzer* IRS spectra assembled for this study. The GTO, GO1, and GO2 spectra all agree with one another within the observational uncertainties except for the region around the $10\ \mu\text{m}$ silicate emission feature. Two additional IRS spectra of CS Cha were taken in GO Program 30300 (PI: Najita) on August 2, 2006. This spectrum was taken using the SH and LH modules. We find that the SH spectrum agrees with our GTO data (taken in July 2005) at $\lambda < 13\ \mu\text{m}$ within the observational uncertainties. The SH spectrum is consistent with both our GTO and GO observations at $\lambda > 13\ \mu\text{m}$. The LH spectrum is consistent with our GTO and GO observations.

We found that we could fit the IRS spectrum well with a 38 AU hole and a silicate dust mixture in the outer wall and disk listed in Table 4 (Figure 16, bottom left; GTO fit: solid line; GO1/GO2 fit: broken line). The optically thin dust region extends up to 1 AU in the hole and contains $1 \times 10^{-12}\ M_{\odot}$ of $0.005\text{--}4\ \mu\text{m}$ dust composed of 15% organics, 11% troilite, and 74% silicates (see Table 5). We note that the size and location of the optically thin region was calculated without taking into account at which radii dust can exist unperturbed in a binary system. However, lacking near-IR interferometry and sufficient details on the orbit of the CS Cha system, we do not pursue this further.

The only variability observed occurs around the $10\ \mu\text{m}$ silicate emission feature. Relative to the time the GTO spectrum was taken, this silicate emission has increased in the GO spectra. This can be explained by increasing the amount of dust in the optically thin inner region by 17%. In Figure 16 (bottom, right panel) we present the best fit model to the broad-band SED. Disk properties can be found in Table 3.

DM Tau

DM Tau was previously modeled in detail by Calvet et al. (2005). They found it had an inner disk hole of 3 AU that was empty of small dust grains. Veiling analysis using near-infrared spectra by Espaillat et al. (2010) confirmed that the inner disk of this object was devoid of sub-micron or micron-sized dust grains. Here we take the model presented in this previous work and modify it to better fit the silicate dust features in the SED and the observed variability.

Figure 17 (top, left) shows the three *Spitzer* IRS spectra assembled for this study. The GTO, GO1, and GO2 spectra all agree with one another.

Eight additional SL spectra of DM Tau were taken in GO Programs 20755 and 30896 (PI: Bary) in September 12, 2005, October 2005, March 2006, October 2006, and March 2007. Two additional high resolution spectra were taken in GO Program 30300 (PI: Najita) on March 14, 2006 using SH and LH. One additional LH spectra was taken by GTO Program 50498 (PI: Houck) on November 10, 2008. We find no variability between these spectra and those in this paper within the observational uncertainties. We note that several campaigns in Program 20755 suffered from mispointing. Since no LL spectra were taken, we cannot discern the degree to which the spectra were affected. Therefore, we do not consider the decrease in flux in the mispointed observations to be intrinsic to the source.

We fit the IRS spectrum with a 3 AU hole and the silicate dust mixture listed in Table 4 (Figure 17, top left, solid line). There is no optically thin dust within the gap. This may be the reason why no variability is observed in this object. In the top right panel of Figure 17 we present the best fit model to the broad-band SED. Disk model properties are listed in Table 3.

T25

T25 is a transitional disk in the Chamaeleon cloud, previously identified by Kim et al. (2009). Here we present the first detailed modeling of this object. Figure 17 (bottom left) shows the three *Spitzer* IRS spectra assembled for this study. The GTO, GO1, and GO2 spectra all agree with one another. Two additional IRS spectra of T25 were taken in GO Program 30300 (PI: Najita) on June 21, 2007 with the SH and LH modules. We find no variability between these spectra and those in this paper within the observational uncertainties.

Using the silicate dust mixture listed in Table 4 and a hole of 13 AU, we modeled the contribution to the SED from the outer wall and disk (Figure 17, bottom left, solid line). The optically thin dust region extends up to 1 AU in the hole and contains ISM-sized dust composed of 19% organics, 15% troilite, and 66% silicates. The silicates are made up of olivines. The gap contains $1 \times 10^{-13} M_{\odot}$ of small optically thin dust, the smallest amount of such dust seen in this sample. This reflects the fact that the $10 \mu\text{m}$ silicate emission feature is very weak. The SNR in this region is also very low and follow-up observations probing if there is indeed $10 \mu\text{m}$ silicate emission in this object would be useful. The combination of the weak silicate emission feature and poor SNR at these wavelengths makes our derivation of the silicate composition in the optically thin inner region more uncertain.

In the middle right panel of Figure 17 we present the best fit model to the broad-band SED. Derived disk parameters are listed in Table 3. We could only find a millimeter upper limit from Henning et al. (1993) which is not useful in constraining the outer disk. In this object, mostly all of the excess emission above the stellar photosphere in the IRS wavelength range can be attributed to the outer wall.

REFERENCES

- Ábrahám, P., et al. 2009, *Nature*, 459, 224
- Aguilar, L. A., Pichardo, B. S., & Sparke, L. S. 2008, in *Revista Mexicana de Astronomía y Astrofísica Conference Series*, Vol. 34, *Revista Mexicana de Astronomía y Astrofísica Conference Series*, 91–97
- Andrews, S. M., & Williams, J. P. 2005, *ApJ*, 631, 1134
- . 2007, *ApJ*, 659, 705
- Andrews, S. M., Wilner, D. J., Hughes, A. M., Qi, C., & Dullemond, C. P. 2009, *ApJ*, 700, 1502
- Artymowicz, P., & Lubow, S. H. 1994, *ApJ*, 421, 651
- Bary, J. S., Leisenring, J. M., & Skrutskie, M. F. 2009, *ApJ*, 706, L168
- Beckwith, S. V. W., & Sargent, A. I. 1991, *ApJ*, 381, 250
- Beckwith, S. V. W., Sargent, A. I., Chini, R. S., & Guesten, R. 1990, *AJ*, 99, 924
- Begemann, B., Dorschner, J., Henning, T., Mutschke, H., & Thamm, E. 1994, *ApJ*, 423, L71
- Bertout, C., Robichon, N., & Arenou, F. 1999, *A&A*, 352, 574
- Bohren, C. F., & Huffman, D. R. 1983, *Absorption and scattering of light by small particles*, ed. Bohren, C. F. & Huffman, D. R.
- Bouwman, J., et al. 2008, *ApJ*, 683, 479
- Boss, A. P. 2004, *ApJ*, 616, 1265
- Boss, A. P., & Durisen, R. H. 2005, *ApJ*, 621, L137
- Calvet, N., D'Alessio, P., Hartmann, L., Wilner, D., Walsh, A., & Sitko, M. 2002, *ApJ*, 568, 1008
- Calvet, N., Muzerolle, J., Briceño, C., Hernández, J., Hartmann, L., Saucedo, J. L., & Gordon, K. D. 2004, *AJ*, 128, 1294
- Calvet, N., et al. 2005, *ApJ*, 630, L185
- Carpenter, J. M., Hillenbrand, L. A., & Skrutskie, M. F. 2001, *AJ*, 121, 3160
- Ciesla, F. J. 2007, *Science*, 318, 613
- Cohen, M., Megeath, S. T., Hammersley, P. L., Martín-Luis, F., & Stauffer, J. 2003, *AJ*, 125, 2645
- D'Alessio, P., Calvet, N., & Hartmann, L. 2001, *ApJ*, 553, 321
- D'Alessio, P., Calvet, N., Hartmann, L., Franco-Hernández, R., & Servín, H. 2006, *ApJ*, 638, 314
- D'Alessio, P., Calvet, N., Hartmann, L., Lizano, S., & Cantó, J. 1999, *ApJ*, 527, 893
- D'Alessio, P., Canto, J., Calvet, N., & Lizano, S. 1998, *ApJ*, 500, 411
- D'Alessio, P., et al. 2005, *ApJ*, 621, 461
- D'Angelo, G., Lubow, S. H., & Bate, M. R. 2006, *ApJ*, 652, 1698
- Desch, S. J., Ciesla, F. J., Hood, L. L., & Nakamoto, T. 2005, in *Astronomical Society of the Pacific Conference Series*, Vol. 341, *Chondrites and the Protoplanetary Disk*, ed. A. N. Krot, E. R. D. Scott, & B. Reipurth, 849–+
- Dorschner, J., Begemann, B., Henning, T., Jaeger, C., & Mutschke, H. 1995, *A&A*, 300, 503
- Dullemond, C. P., & Dominik, C. 2004, *A&A*, 417, 159
- Dutrey, A., Guilloteau, S., Duvert, G., Prato, L., Simon, M., Schuster, K., & Menard, F. 1996, *A&A*, 309, 493
- Dutrey, A., Guilloteau, S., Prato, L., Simon, M., Duvert, G., Schuster, K., & Menard, F. 1998, *A&A*, 338, L63
- Egan, W., & Hilgeman, T. 1977, *Icarus*, 30, 413
- Eiroa, C., et al. 2002, *A&A*, 384, 1038
- Espaillat, C. 2009, PhD thesis, University of Michigan
- Espaillat, C., Calvet, N., D'Alessio, P., Hernández, J., Qi, C., Hartmann, L., Furlan, E., & Watson, D. M. 2007a, *ApJ*, 670, L135
- Espaillat, C., Calvet, N., Luhman, K. L., Muzerolle, J., & D'Alessio, P. 2008a, *ApJ*, 682, L125
- Espaillat, C., et al. 2007b, *ApJ*, 664, L111
- . 2008b, *ApJ*, 689, L145
- . 2010, *ApJ*, 717, 441
- Fabian, D., Henning, T., Jäger, C., Mutschke, H., Dorschner, J., & Wehrhan, O. 2001, *A&A*, 378, 228
- Flaherty, K. M., & Muzerolle, J. 2010, *ApJ*, 719, 1733
- Furlan, E., et al. 2006, *ApJS*, 165, 568
- . 2009, *ApJ*, 703, 1964
- Gail, H. 2004, *A&A*, 413, 571
- Gail, H.-P. 2001, *A&A*, 378, 192
- Gauvin, L. S., & Strom, K. M. 1992, *ApJ*, 385, 217
- Gervais, F., & Piriou, B. 1975, *Phys. Rev. B*, 11, 3944
- Guenther, E. W., Esposito, M., Mundt, R., Covino, E., Alcalá, J. M., Cusano, F., & Stecklum, B. 2007, *A&A*, 467, 1147
- Gullbring, E., Hartmann, L., Briceno, C., & Calvet, N. 1998, *ApJ*, 492, 323
- Hartigan, P., Hartmann, L., Kenyon, S., Hewett, R., & Stauffer, J. 1989, *ApJS*, 70, 899
- Henning, T., & Mutschke, H. 1997, *A&A*, 327, 743
- Henning, T., Pfau, W., Zinnecker, H., & Prusti, T. 1993, *A&A*, 276, 129
- Herbig, G. H., Vrba, F. J., & Rydgren, A. E. 1986, *AJ*, 91, 575
- Higdon, S. J. U., et al. 2004, *PASP*, 116, 975
- Houck, J. R., et al. 2004, *ApJS*, 154, 18
- Huffman, D. R., & Stapp, J. L. 1971, *Nature*, 229, 45
- Hughes, A. M., Wilner, D. J., Calvet, N., D'Alessio, P., Claussen, M. J., & Hogerheijde, M. R. 2007, *ApJ*, 664, 536
- Hughes, A. M., et al. 2009, *ApJ*, 698, 131
- Isella, A., Carpenter, J. M., & Sargent, A. I. 2010, *ApJ*, 714, 1746
- Jaeger, C., Molster, F. J., Dorschner, J., Henning, T., Mutschke, H., & Waters, L. B. F. M. 1998, *A&A*, 339, 904
- Jaeger, C., Mutschke, H., Begemann, B., Dorschner, J., & Henning, T. 1994, *A&A*, 292, 641
- Joy, A. H. 1945, *ApJ*, 102, 168
- . 1949, *ApJ*, 110, 424
- Juhász, A., Prusti, T., Ábrahám, P., & Dullemond, C. P. 2007, *MNRAS*, 374, 1242
- Keller, C., & Gail, H.-P. 2004, *A&A*, 415, 1177
- Kenyon, S. J., & Hartmann, L. 1995, *ApJS*, 101, 117
- Kim, K. H., et al. 2009, *ApJ*, 700, 1017
- Kitamura, Y., Momose, M., Yokogawa, S., Kawabe, R., Tamura, M., & Ida, S. 2002, *ApJ*, 581, 357
- Koerner, D. W., Sargent, A. I., & Beckwith, S. V. W. 1993, *Icarus*, 106, 2
- Loewenstein, E. V., Smith, D. R., & Morgan, R. L. 1973, *Appl. Opt.*, 12, 398
- Lommen, D., Maddison, S. T., Wright, C. M., van Dishoeck, E. F., Wilner, D. J., & Bourke, T. L. 2009, *A&A*, 495, 869

- Lommen, D., et al. 2007, *A&A*, 462, 211
- Lommen, D. J. P. 2009, PhD thesis, Leiden Observatory, Leiden University, P.O. Box 9513, 2300 RA Leiden, The Netherlands
- Looney, L. W., Mundy, L. G., & Welch, W. J. 2000, *ApJ*, 529, 477
- Lubow, S. H., & D’Angelo, G. 2006, *ApJ*, 641, 526
- Luhman, K. L. 2004, *ApJ*, 602, 816
- Luhman, K. L. 2007, *ApJS*, 173, 104
- Luhman, K. L., Allen, P. R., Espaillat, C., Hartmann, L., & Calvet, N. 2010, *ApJS*, 186, 111
- Luhman, K. L., et al. 2008, *ApJ*, 675, 1375
- Marcy, G., Butler, R. P., Fischer, D., Vogt, S., Wright, J. T., Tinney, C. G., & Jones, H. R. A. 2005, *Progress of Theoretical Physics Supplement*, 158, 24
- Mathis, J. S. 1990, *ARA&A*, 28, 37
- Mathis, J. S., Rumpl, W., & Nordsieck, K. H. 1977, *ApJ*, 217, 425
- McCabe, C., Ghez, A. M., Prato, L., Duchêne, G., Fisher, R. S., & Telesco, C. 2006, *ApJ*, 636, 932
- Min, M., Waters, L. B. F. M., de Koter, A., Hovenier, J. W., Keller, L. P., & Markwick-Kemper, F. 2007, *A&A*, 462, 667
- Monet, D. G. 1998, in *Bulletin of the American Astronomical Society*, Vol. 30, *Bulletin of the American Astronomical Society*, 1427–+
- Mulders, G. D., Dominik, C., & Min, M. 2010, *A&A*, 512, A11+
- Muzerolle, J., D’Alessio, P., Calvet, N., & Hartmann, L. 2004, *ApJ*, 617, 406
- Muzerolle, J., et al. 2009, *ApJ*, 704, L15
- Nagel, E., D’Alessio, P., Calvet, N., Espaillat, C., Sargent, B., Hernández, J., & Forrest, W. J. 2010, *ApJ*, 708, 38
- Olofsson, J., Augereau, J., van Dishoeck, E. F., Merin, B., Grosso, N., Ménard, F., Blake, G. A., & Monin, J. 2010, *ArXiv e-prints*
- Olofsson, J., et al. 2009, *A&A*, 507, 327
- Palik, E. D. 1985, *Handbook of optical constants of solids*, ed. Palik, E. D.
- Pichardo, B., Sparke, L. S., & Aguilar, L. A. 2005, *MNRAS*, 359, 521
- Piétu, V., Dutrey, A., Guilloteau, S., Chapillon, E., & Pety, J. 2006, *A&A*, 460, L43
- Pollack, J. B., Hollenbach, D., Beckwith, S., Simonelli, D. P., Roush, T., & Fong, W. 1994, *ApJ*, 421, 615
- Poteet, C. e. a. 2010, submitted
- Rebull, L. M., et al. 2010, *ApJS*, 186, 259
- Rice, W. K. M., Armitage, P. J., & Hogg, D. F. 2008, *MNRAS*, 384, 1242
- Rice, W. K. M., Armitage, P. J., Wood, K., & Lodato, G. 2006, *MNRAS*, 373, 1619
- Rodmann, J., Henning, T., Chandler, C. J., Mundy, L. G., & Wilner, D. J. 2006, *A&A*, 446, 211
- Rydgren, A. E. 1980, *AJ*, 85, 444
- Rydgren, A. E., Strom, S. E., & Strom, K. M. 1976, *ApJS*, 30, 307
- Sargent, B. A., et al. 2009, *ApJS*, 182, 477
- Siess, L., Dufour, E., & Forestini, M. 2000, *A&A*, 358, 593
- Simon, M., Dutrey, A., & Guilloteau, S. 2000, *ApJ*, 545, 1034
- Sitko, M. L., et al. 2008, *ApJ*, 678, 1070
- Skrutskie, M. F., Meyer, M. R., Whalen, D., & Hamilton, C. 1996, *AJ*, 112, 2168
- Skrutskie, M. F., et al. 2006, *AJ*, 131, 1163
- Strom, K. M., Strom, S. E., Edwards, S., Cabrit, S., & Skrutskie, M. F. 1989, *AJ*, 97, 1451
- Swain, M. R., Bouwman, J., Akeson, R. L., Lawler, S., & Beichman, C. A. 2008, *ApJ*, 674, 482
- Turner, N. J., Carballido, A., & Sano, T. 2010, *ApJ*, 708, 188
- Warren, S. G. 1984, *Appl. Opt.*, 23, 1206
- Watson, D. M., et al. 2009, *ApJS*, 180, 84
- Weaver, W. B., & Jones, G. 1992, *ApJS*, 78, 239
- Weintraub, D. A., Sandell, G., & Duncan, W. D. 1989, *ApJ*, 340, L69
- Werner, M. W., et al. 2004, *ApJS*, 154, 1
- White, R. J., & Ghez, A. M. 2001, *ApJ*, 556, 265
- Whittet, D. C. B., Prusti, T., Franco, G. A. P., Gerakines, P. A., Kilkenny, D., Larson, K. A., & Wesselius, P. R. 1997, *A&A*, 327, 1194
- Zhu, Z., Nelson, R., Hartmann, L., Espaillat, C., & Calvet, N. 2010, submitted to *ApJ*

Table 1
Log of Observations

Target	Alt. Names	Label	Date	AOR ID
CR Cha	T 8	GTO	2005-05-26	12697345
...	SZ 6	GO1	2008-06-01	26143744
...	CHX 3	GO2	2008-06-08	27186944
CS Cha	T 11	GTO	2005-07-11	12695808
...		GO1	2008-06-01	26144000
...		GO2	2008-06-08	27187712
DM Tau		GTO1	2004-02-08	3536384
...		GTO2	2006-03-15	16346624
...		GO1	2008-10-01	26141952
...		GO2	2008-10-08	27184640
GM Aur		GTO	2004-02-27	3538944
...		GO1	2008-10-07	26141696
...		GO2	2008-10-14	27186688
IP Tau		GTO	2004-02-08	3535616
...		GO1	2008-10-02	26141440
...		GO2	2008-10-08	27184896
ISO 52	B18	GTO	2005-07-12	12691200
...		GO1	2008-06-01	26144768
...		GO2	2008-06-08	27187200
LkCa 15		GTO	2004-02-08	3537664
...		GO1	2008-10-02	26140672
...		GO2	2008-10-08	27186176
RY Tau		GTO ^a	2004-03-02	3529984
...		GO1 ^b	2008-10-07	26141184
...		GO2 ^b	2008-10-14	27185920
SZ Cha	T6	GTO	2005-07-12	12696832
...		GO1	2008-06-01	26142464
...		GO2	2008-06-08	27187968
T25	SZ 18	GTO	2005-04-24	1269552
...		GO1	2008-06-01	26144256
...		GO2	2008-06-08	27185152
T35	SZ 27	GTO	2005-07-13	12696320
...		GO1	2008-06-01	26143488
...		GO2	2008-06-08	27185664
T56	SZ 45	GTO	2005-07-13	12696064
...	HM 32	GO1	2008-06-01	26142720
...		GO2	2008-06-08	27186432
UX Tau A		GTO	2004-02-08	3536384
...		GO1	2008-10-01	26140928
...		GO2	2008-10-08	27187456
WW Cha	T44	GTO	2006-03-07	12697088
...	SZ 34	GO1 ^a	2008-06-01	26142976
...		GO2 ^a	2008-06-09	27185408

^a These observations were slightly mispointed.

^b These spectra were saturated in the 10 μm region.

Table 2
Stellar Properties of Sample

Target	A_V	Spectral Type	T_* (K)	L_* (M_\odot)	M_* (M_\odot)	R_* (R_\odot)	\dot{M} ($10^{-9} M_\odot \text{ yr}^{-1}$)	Distance (pc)
CR Cha	1.5	K2 ^b	4900	3.5	1.9	2.6	8.8	160
CS Cha	0.8	K6 ^a	4205	1.5	0.9	2.3	12	160
DM Tau	0.7	M1.5 ^c	3720	0.3	0.5	1.3	3.1	140
GM Aur	0.8	K5.5 ^c	4350	0.9	1.1	1.7	4.7	140
IP Tau	0.5	M0 ^d	3850	0.5	0.6	1.6	0.42	140
ISO 52	1.3	M4 ^a	3370	0.1	0.3	1.0	—	160
LkCa 15	1.7	K3 ^c	4730	1.2	1.3	1.6	3.3	140
RY Tau	2.2	G1 ^e	5945	11.7	2.2	3.2	9 ^e 1	140
SZ Cha	1.9	K0 ^b	5250	1.9	1.4	1.7	2.4	160
T25	1.6	M2.5 ^a	3470	0.3	0.3	1.5	0.97	160
T35	3.5	M0 ^f	3850	0.4	0.6	1.5	1.2	160
T56	0.6	M0.5 ^a	3720	0.4	0.5	1.6	1.5	160
UX Tau A	1.8	G8 ^c	5520	2.6	1.5	1.8	11	140
WW Cha	4.8	K5 ^a	4350	6.5	1.2	4.5	—	160

^a Luhman (2004)

^b Rydgren (1980)

^c Espaillat et al. (2010)

^d Herbig et al. (1986)

^e Calvet et al. (2004)

^f Gauvin & Strom (1992)

Table 3
Disk Properties of Sample

Target	i	Inner Wall ^a				Outer Wall ^a				Outer Disk		
		a_{max} (μm)	T_{wall}^i (K)	z_{wall}^i (AU)	R_{wall}^i (AU)	a_{max} (μm)	T_{wall}^o (K)	z_{wall}^o (AU)	R_{wall}^o (AU)	ϵ	α	M_{disk} (M_{\odot})
CR Cha	60	1	0.25	220	...	10	0.01	0.0013	0.1
CS Cha	60	—	—	—	—	4	90	7	38	0.01	0.001	0.3
DM Tau	45 ^b	—	—	—	—	1	200	0.3	3	0.5	0.001	0.1
GM Aur	64 ^c	—	—	—	—	3	110	2.9(3.2)	23	0.01	0.0004	0.4
IP Tau	60	10	1400	0.006(0.007)	0.07	4	230	36	2	0.01	0.0008	0.01
LkCa 15	42 ^b	1	1400	0.009(0.007)	0.15	0.25	110	5	39	0.001	0.0005	0.1
RY Tau	71 ^d	10	1400	0.02	0.42	3	220	4	18	0.01	0.01	0.2
SZ Cha	60	5	1400	0.006(0.008)	0.16	4	135	4	18	0.01	0.001	0.05
T25	60	—	—	—	—	5	100	2	13	—	—	—
T35	60	10	1800	0.005(0.006)	0.04	3	100	4	15	—	—	—
T56	60	10	1400	0.002(0.001)	0.06	0.25	100	4	20	0.001	0.0001	0.3
UX Tau A	60	10	1550	0.006(0.005)	0.15	5	120	3	30	0.001	0.004	0.05

^a For the wall heights, the values given correspond to the best fit to the GTO spectrum. The values relevant to the GO1 spectra are in parenthesis. For CR Cha, see the Appendix for the values of the inner wall temperature, height, and radius and the height of the outer wall. In the case of UX Tau A, we do not fit the GTO spectrum. Instead we list the height of the inner wall for the GO1 spectrum; the value for the GO2 spectrum is in parenthesis. All other parameter values listed are the same between all the epochs.

^b Simon et al. (2000)

^c Hughes et al. (2009)

^d Isella et al. (2010)

Table 4
Mass Fraction (in %) of Silicates in Outer Wall & Disk

Target	Amorphous Olivine	Amorphous Pyroxene	Crystalline Forsterite	Crystalline Enstatite	Crystalline Silica
CR Cha	—	90	—	—	10
CS Cha	—	98	2	—	—
DM Tau	65	30	2	—	3
GM Aur	45	50	—	—	5
IP Tau	50	45	5	—	—
ISO 52	80	—	10	10	—
LkCa 15	88	—	1	—	11
RY Tau	100	—	—	—	—
SZ Cha	32	55	5	1	7
T25	90	—	10	—	—
T35	40	—	30	30	—
T56	—	82	8	—	10
UX Tau A	81	—	10	4	5

Table 5
Mass Fraction (in %) of Silicates in Optically Thin Dust Region

Target	Amorphous Olivine	Amorphous Pyroxene	Crystalline Forsterite	Crystalline Enstatite	Crystalline Silica
CR Cha	—	90	—	—	10
CS Cha	95	—	—	5	—
GM Aur	90	—	10	—	—
IP Tau	50	45	5	—	—
ISO 52	80	—	10	10	—
LkCa 15 ^a	90	—	10	—	—
LkCa 15 ^b	—	100	—	—	—
RY Tau	100	—	—	—	—
SZ Cha	90	—	10	—	—
T25	100	—	—	—	—
T56	41	34	10	15	—

^b Values are for optically thin dust located within 1 AU of the gap.

^c Values are for optically thin dust located between 1 and 15 AU of the gap.

Table 6
Spitzer Photometry

Target	Instrument ^a	Date	Symbol ^b
CR Cha	—	—	—
CS Cha	IRAC	01 May 2004	
...	IRAC	04 Jul 2004	open blue
...	IRAC	10 Jul 2006	open red
...	MIPS 24 μm	08 Apr 2004	
...	MIPS 24 μm	22 Jun 2004	open blue
...	MIPS 24 μm	27 Feb 2005	open red
DM Tau	IRAC	19 Feb 2005	
GM Aur	IRAC	14 Feb 2004	
...	MIPS 24 μm	05 Mar 2005	
IP Tau	IRAC	20 Feb 2005	
...	IRAC	21 Feb 2005	open blue
...	IRAC	16 Oct 2007	open red
...	MIPS 70 μm	27 Feb 2005	
ISO 52	IRAC	19 Feb 2004	
...	IRAC	10 Jun 2004	open red
...	IRAC	09 Jul 2004	open green
...	IRAC	02 Sep 2004	open magenta
...	MIPS 24 μm	08 Apr 2004	
...	MIPS 24 μm	27 Feb 2005	open red
LkCa 15	IRAC	20 Feb 2005	
...	IRAC	3 Apr 3 2007	open blue
...	MIPS 24 μm	26 Feb 2007	
...	MIPS 70 μm	27 Feb 2007	
RY Tau	IRAC	20 Feb 2005	
...	IRAC	21 Feb 2005	open blue
SZ Cha	IRAC	10 Jul 2006	
T25	IRAC	10 Jul 2006	
T35	IRAC	10 Jun 2004	
...	MIPS 24 μm	27 Feb 2005	
T56	—	—	—
UX Tau A	IRAC	19 Feb 2005	
...	MIPS 24 μm	25 Sept 2004	
WW Cha	IRAC	04 Jul 2004	

^a IRAC and MIPS 24 μm photometry for objects in Taurus are from Luhman et al. (2010); for Chamaeleon objects, these data are from Luhman et al. (2008). All MIPS 70 μm photometry are taken from Rebull et al. (2010)

^b All IRAC and MIPS photometry are plotted as closed, blue triangles unless otherwise noted.

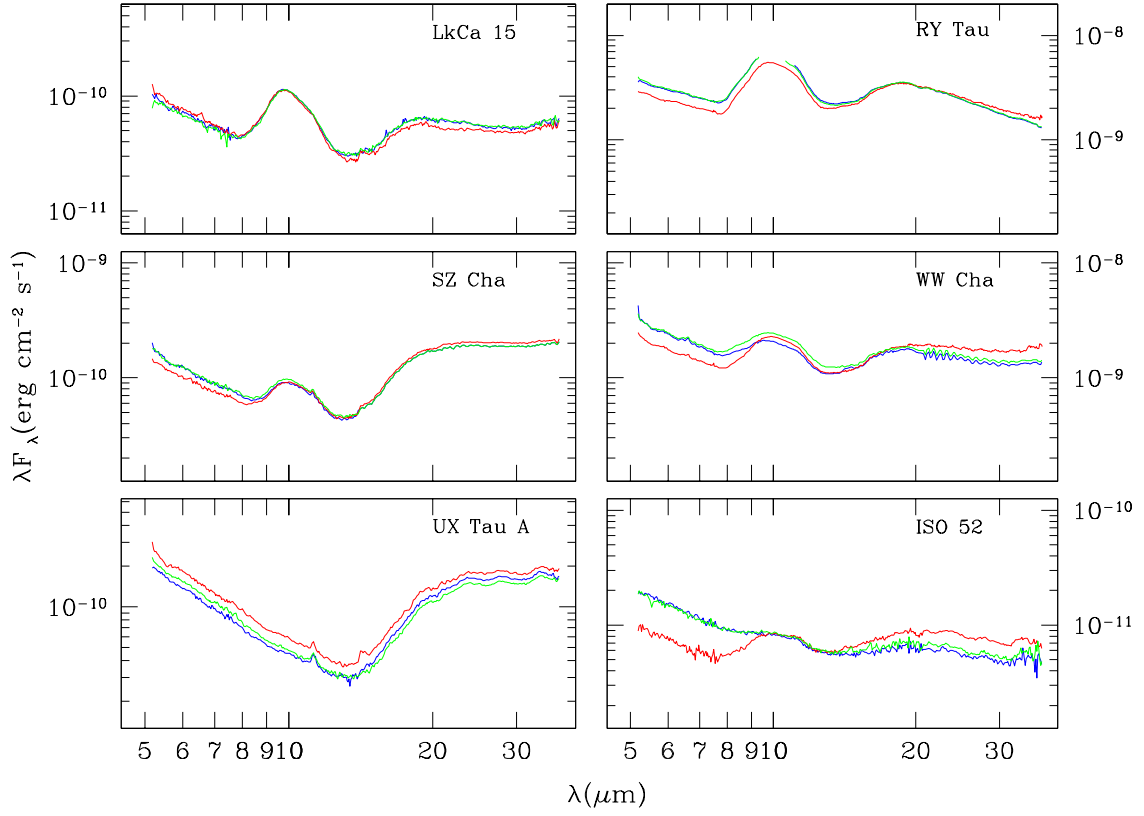


Figure 1. *Spitzer* IRS spectra for pre-transitional disks in our sample which exhibit seesaw-like behavior. All epochs are shown: GTO (red), GO1 (green), GO2 (blue). Variability is apparent in all the objects. None of the spectra have been corrected for extinction. Note that for RY Tau the region around $10\ \mu\text{m}$ in the GO spectra has been removed since they were saturated in this region. The GTO observations of RY Tau and the GO observations of WW Cha were significantly mispointed and so the variability seen here should be taken as an indication of the overall behavior of the variability in these objects and not as an accurate measurement of the amount of variability. We note that the fringing observed longward of $20\ \mu\text{m}$ in WW Cha is due to mispointing. (A color version of this figure is available in the online journal.)

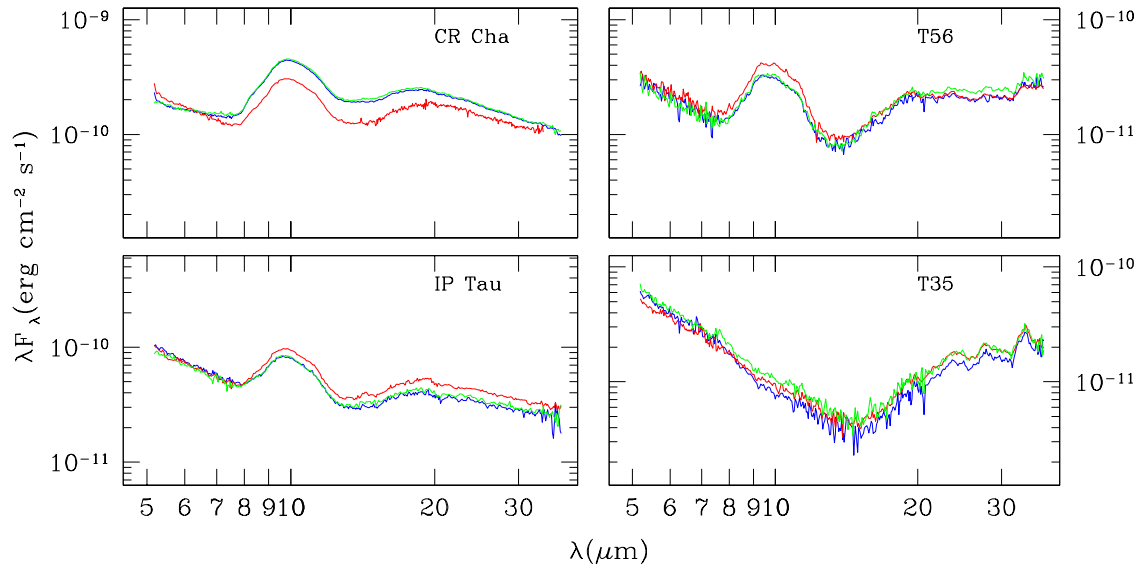


Figure 2. *Spitzer* IRS spectra for pre-transitional disks in our sample where there is no clear pivot point. The color scheme is the same as that used in Figure 1. (A color version of this figure is available in the online journal.)

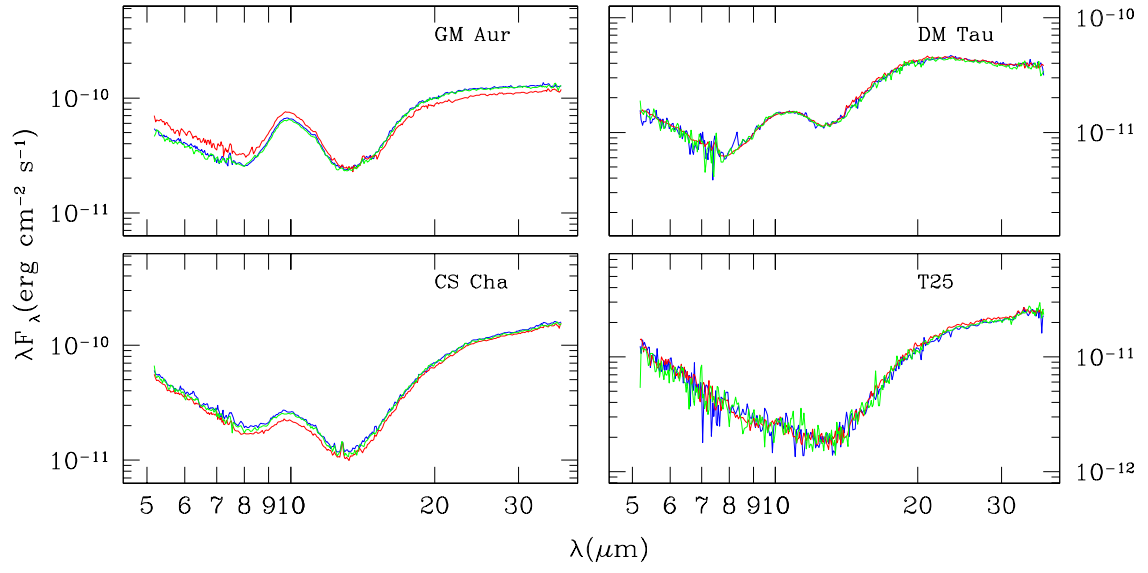


Figure 3. *Spitzer* IRS spectra for the transitional disks in our sample. The color scheme is the same as that used in Figure 1. No variability is observed in DM Tau and T25. (A color version of this figure is available in the online journal.)

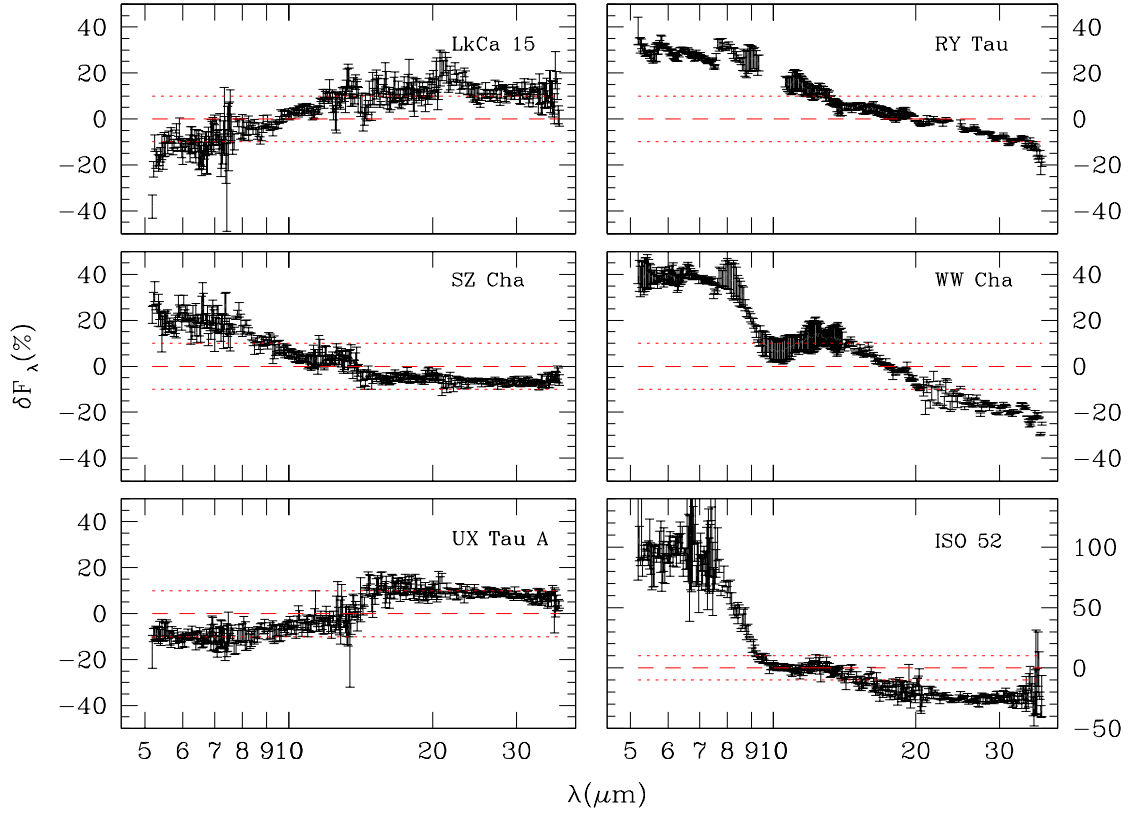


Figure 4. Variability observed in the objects shown in Figure 1. Here we show the percentage change in flux between our GTO and GO1 spectra (i.e. $100 \times (F_{\lambda,GO1} - F_{\lambda,GTO}) / F_{\lambda,GTO}$). The error bars correspond to the uncertainties in the observations. The dashed line corresponds to no change in flux (i.e. $\delta F_{\lambda} \sim 0$) and the dotted lines correspond to a 10% change in flux. In the case of UX Tau A, we show the percentage change in flux between its GO1 and GO2 spectra (i.e. $100 \times (F_{\lambda,GO2} - F_{\lambda,GO1}) / F_{\lambda,GO1}$). Note that the region around $10 \mu\text{m}$ has been removed in RY Tau since its spectra were saturated in this region. The GTO observation of RY Tau and the GO observations of WW Cha were mispointed and so the variability seen here should be taken as an indication of the overall behavior of the variability in these objects and not as an accurate measurement of the amount of variability.

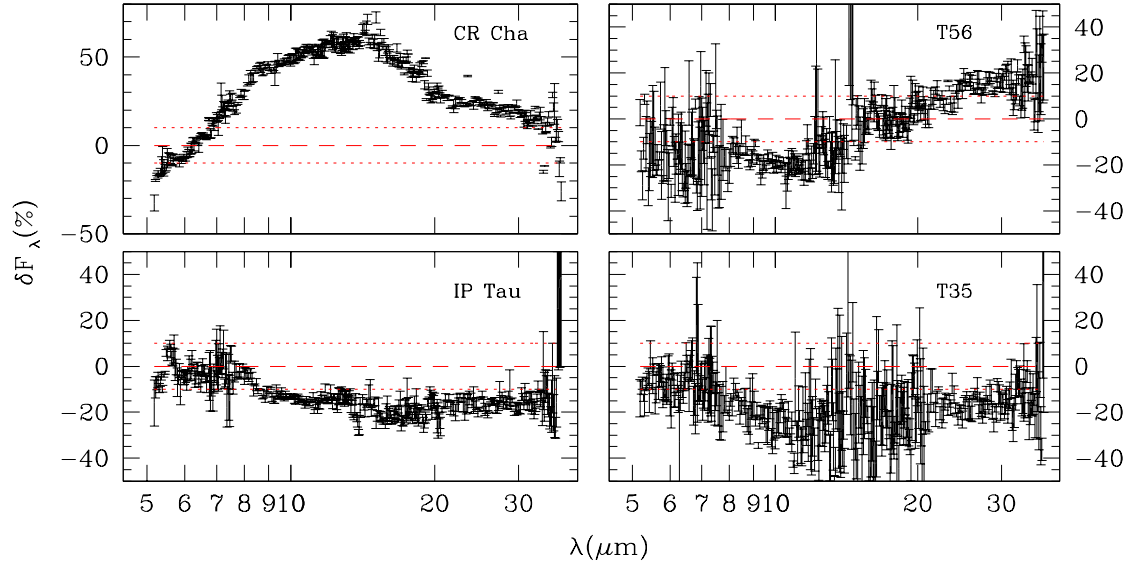


Figure 5. Variability observed in the objects shown in Figure 2. Symbols are the same as in Figure 4. In the case of T35, we show the percentage change in flux between its GO1 and GO2 spectra.

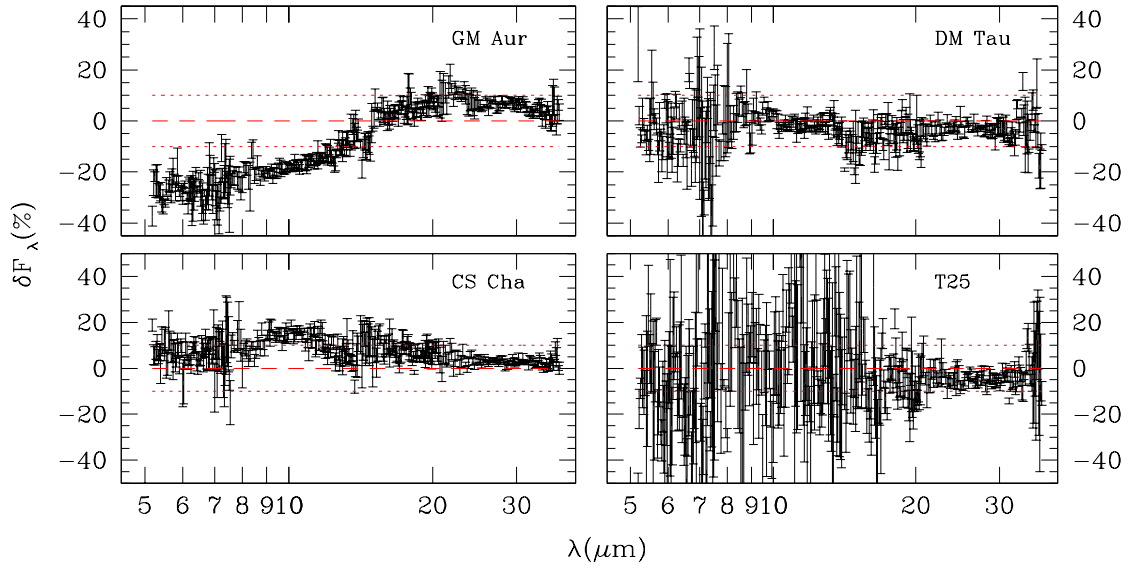


Figure 6. Variability observed in the objects shown in Figure 3. Symbols are the same as in Figure 4. Except in the cases of DM Tau and T25, a $>10\%$ change in flux is observed.

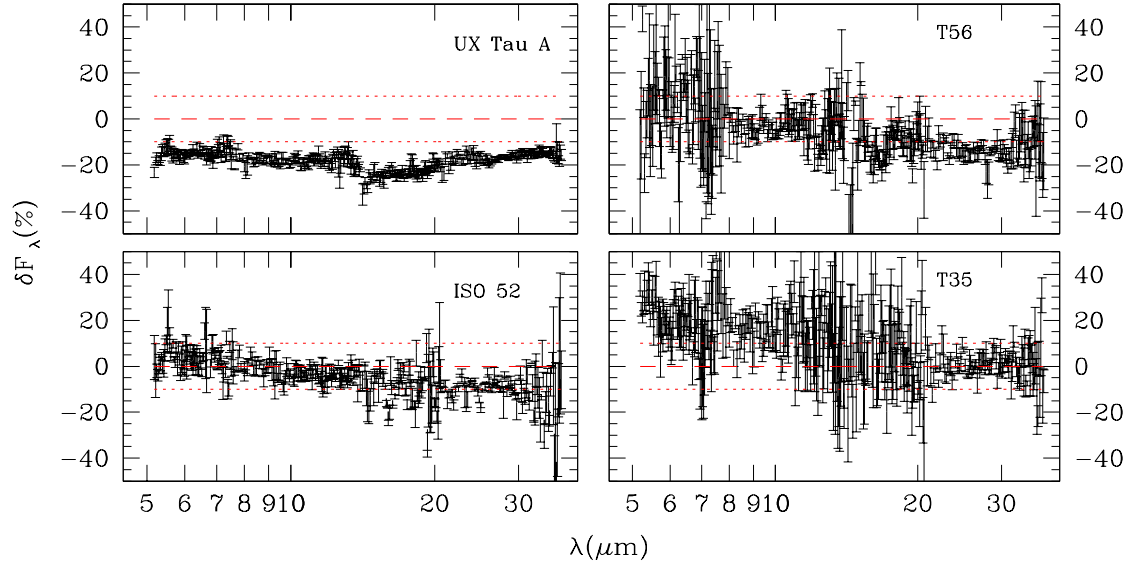


Figure 7. Additional variability observed in UX Tau A, ISO 52, T56, and T35. Here we show the percentage change in flux between the GTO and GO1 spectra for UX Tau A and T35. For ISO 52 and T56 we plot the difference between the GO1 and GO2 spectra.

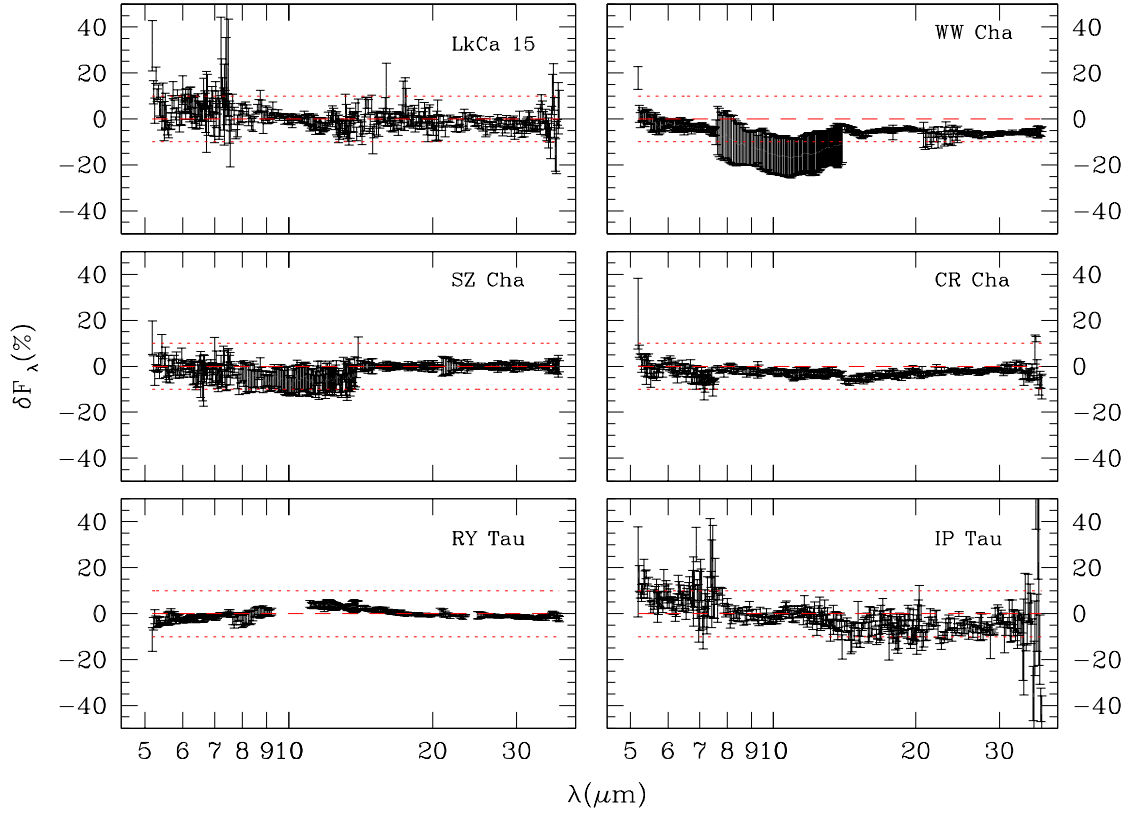


Figure 8. Percentage change in flux between the GO1 and GO2 spectra for some of the pre-transitional disks in the sample. None of these objects vary on this 1 week timescale. We note that the WW Cha observations were significantly mispointed. The percentage change in flux between the GO1 and GO2 observations of UX Tau A, ISO 52, T35, and T56 can be found in Figures 4, 7, 5, and 7, respectively.

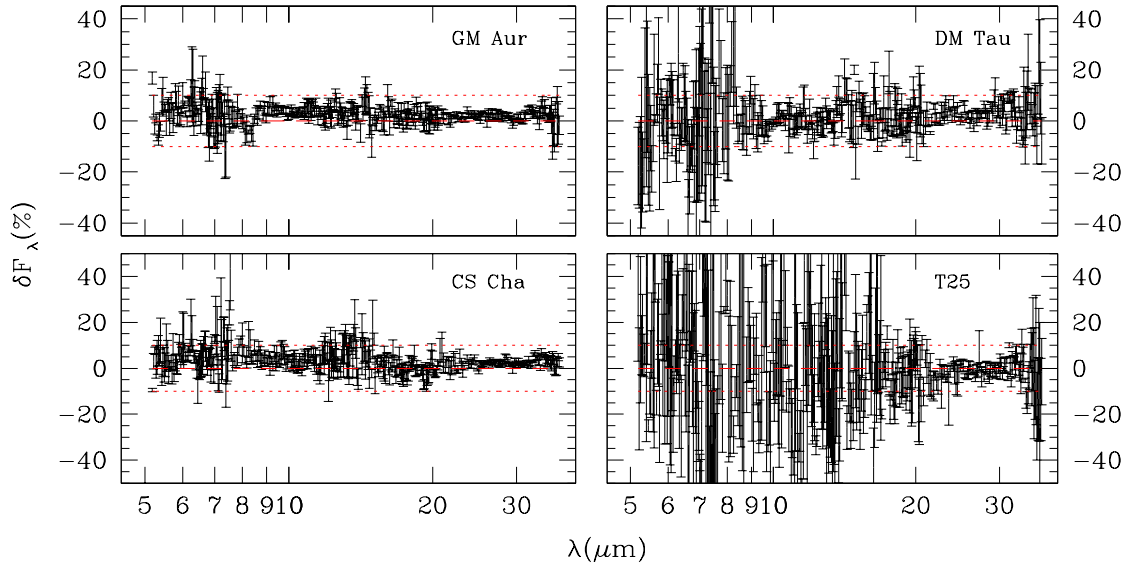


Figure 9. Percentage change in flux between the GO1 and GO2 spectra for the transitional disks in the sample. None of the objects vary on this 1 week timescale.

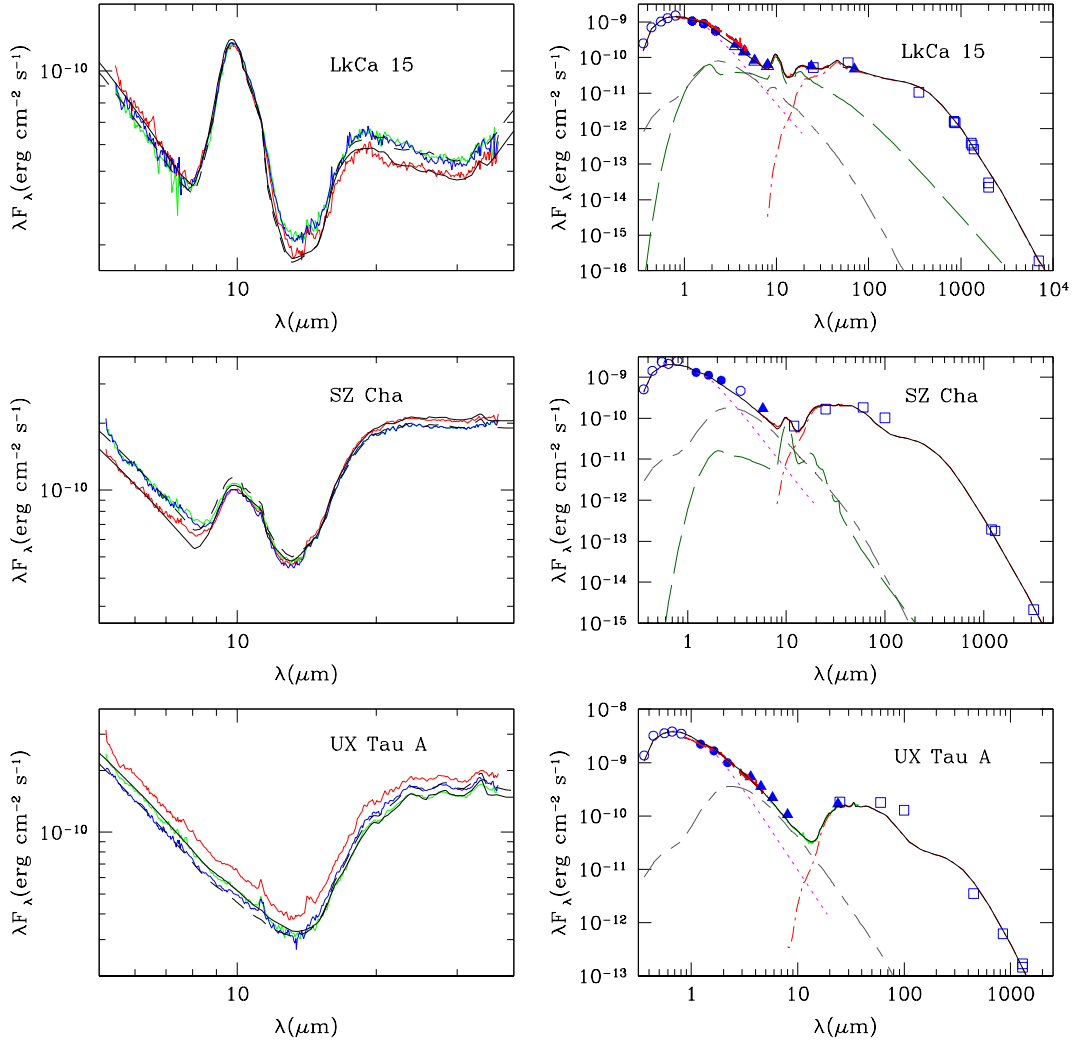


Figure 10. SEDs and disk models of LkCa 15, SZ Cha, and UX Tau A. The left panels show the IRS GTO (red), GO1 (green), and GO2 (blue) spectra for the target plotted with the best fit models (solid and broken black lines; refer to the Appendix for more details). The right panels show the best fit model to the GTO IRS spectrum along with the rest of the broad band SED. In the case of UX Tau A, the best fit to the GO1 spectrum is used. SpeX spectra first presented in Espaillat et al. (2010) are also plotted in the cases of LkCa 15 and UX Tau A. Open circles correspond to ground-based (UBVRIL) photometry; for Taurus these data are taken from Kenyon & Hartmann (1995) and for Chamaeleon we use photometry from Gauvin & Strom (1992). Closed circles are 2MASS photometry from Skrutskie et al. (2006). Triangles are *Spitzer* photometry (see Table 6 for more details). Squares correspond to IRAS and millimeter fluxes. IRAS data are taken from Weaver & Jones (1992). Millimeter data for LkCa 15 are from Andrews & Williams (2005); Espaillat et al. (2007a); Rodmann et al. (2006); Kitamura et al. (2002). Millimeter fluxes for SZ Cha were measured by Henning et al. (1993) and Lommen (2009). UX Tau A's millimeter data are from Andrews & Williams (2005) and Beckwith et al. (1990). The observations have been dereddened using the extinctions listed in Table 3. Separate model components are the stellar photosphere (magenta dotted line; Kenyon & Hartmann 1995), the inner disk (gray short-short-dash), the outer disk (red dot-short-dash), and the optically thin small dust located within the inner disk (green long-dash). (A color version of this figure is available in the online journal.)

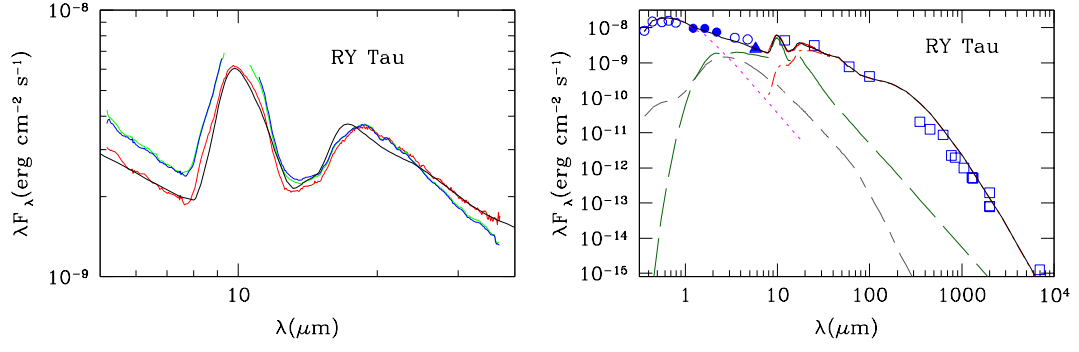


Figure 11. SED and disk model of RY Tau. The left panels show the IRS GTO (red), GO1 (green), and GO2 (blue) spectra for the target plotted with the best fit models (solid and broken black lines; refer to the Appendix for more details). Plotted data are the same as described in Figure 10. Note that for RY Tau the region around $10\ \mu\text{m}$ in the GO spectra has been removed due to saturation. Millimeter data for RY Tau are from Andrews & Williams (2005) and Andrews & Williams (2007). (A color version of this figure is available in the online journal.)

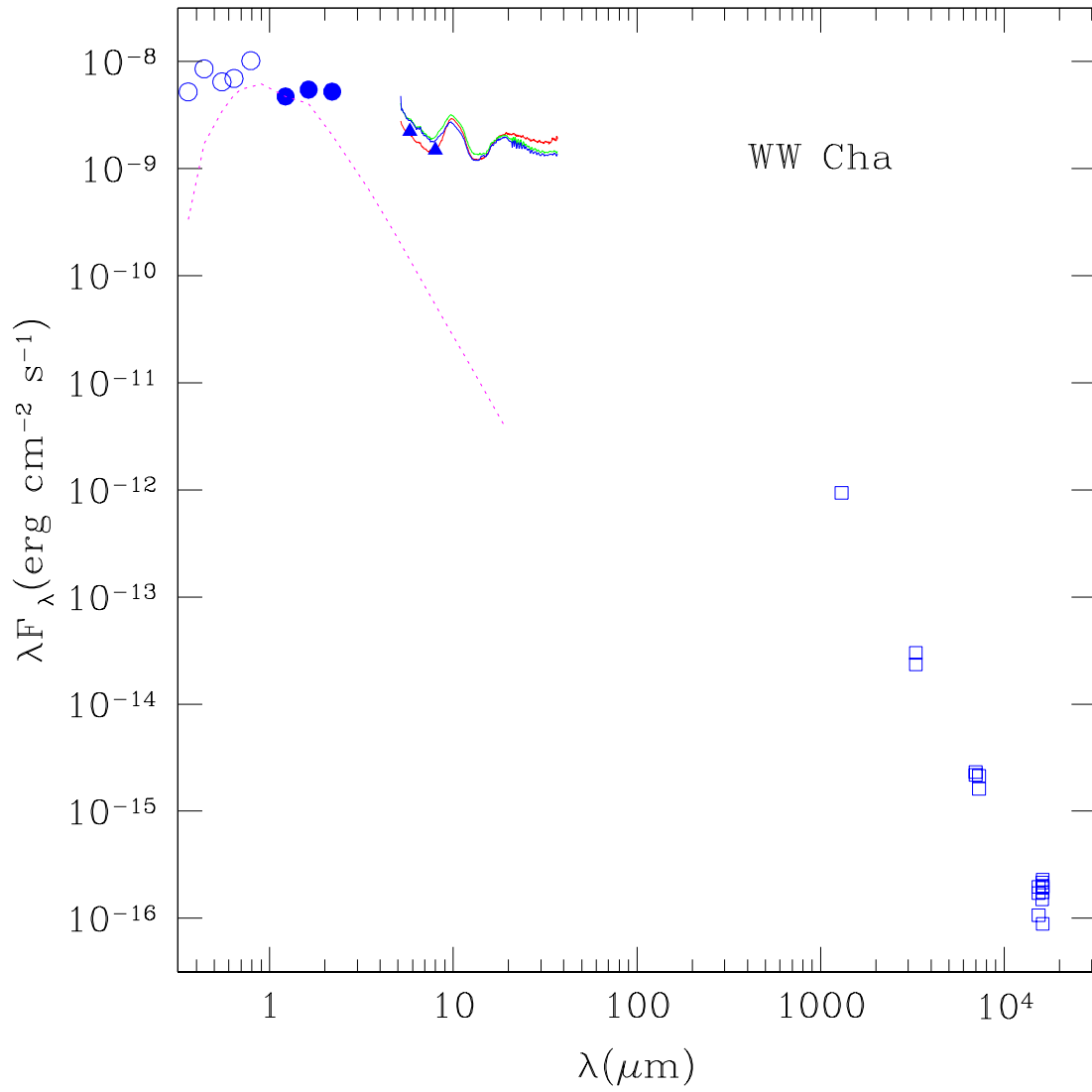


Figure 12. Broad-band SED of WW Cha including the IRS GTO (red), GO1 (green), and GO2 (blue) spectra. See the Appendix for further discussion. Refer to the caption of Figure 10 for more details on the plotted data. Millimeter fluxes are taken from the literature (Henning et al. 1993; Lommen et al. 2007, 2009). (A color version of this figure is available in the online journal.)

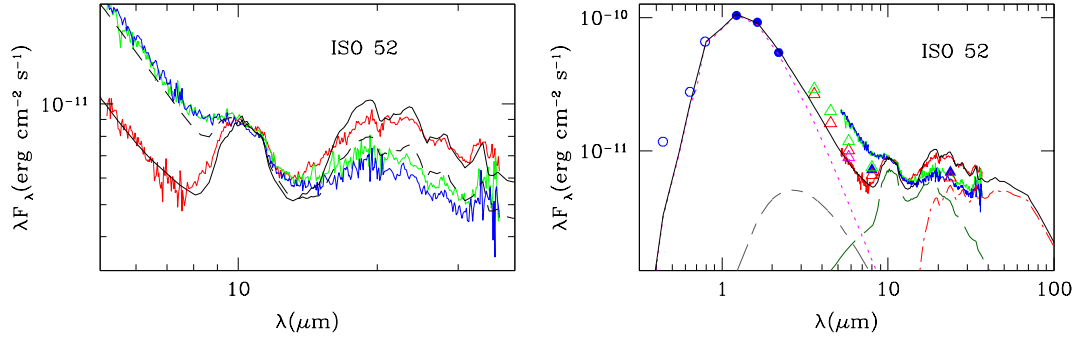


Figure 13. Broad-band SED of ISO 52. The left panels show the IRS GTO (red), GO1 (green), and GO2 (blue) spectra for the target plotted with the best fit models (solid and broken black lines; refer to the Appendix for more details). Refer to the caption of Figure 10 for more details on the plotted data. B and R photometry (open circles) are from Monet (1998). I-band photometry (open circle) is from DENIS. (A color version of this figure is available in the online journal.)

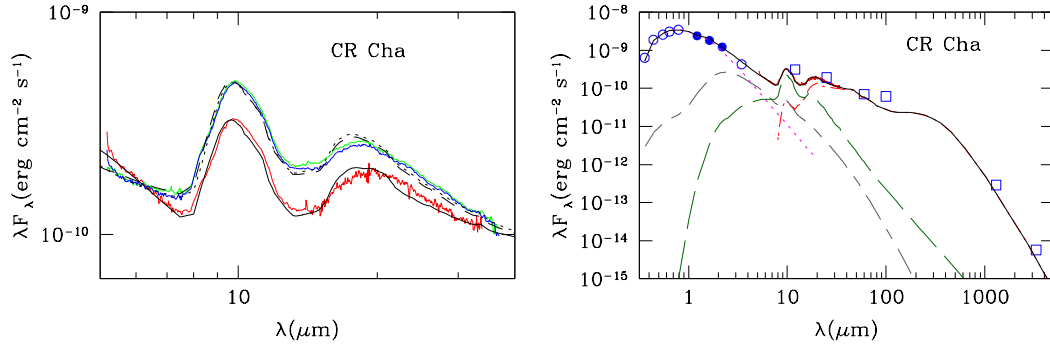


Figure 14. SED and disk model of CR Cha. The left panels show the IRS GTO (red), GO1 (green), and GO2 (blue) spectra for the target plotted with the best fit models (solid and broken black lines; refer to the Appendix for more details). Refer to the caption of Figure 10 for more details on the plotted data. Millimeter fluxes are from Henning et al. (1993) and Lommen et al. (2007). (A color version of this figure is available in the online journal.)

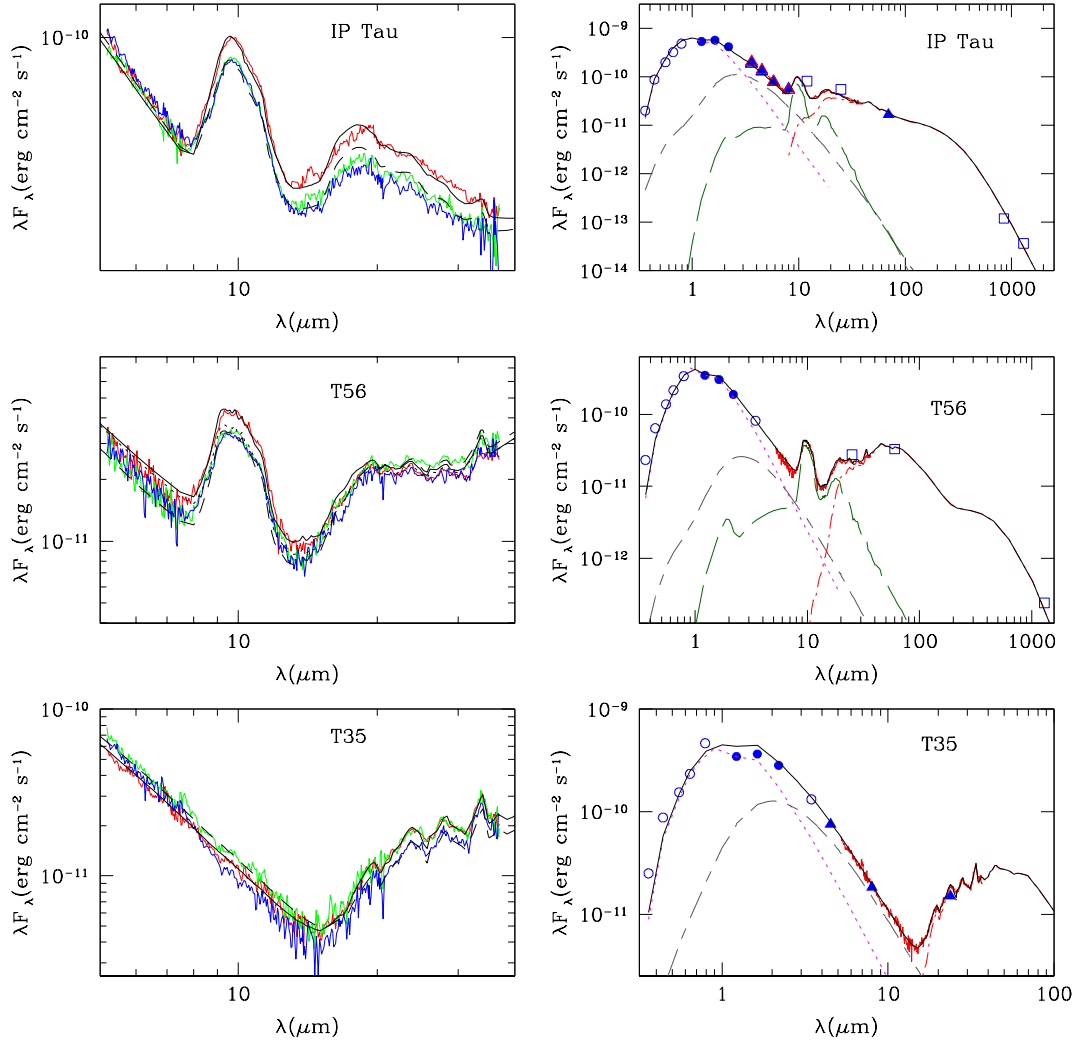


Figure 15. SEDs and disk models of IP Tau, T56, and T35. The left panels show the IRS GTO (red), GO1 (green), and GO2 (blue) spectra for the target plotted with the best fit models (solid and broken black lines; refer to the Appendix for more details). Symbols, data references, and model lines are the same as noted in the caption of Figure 10. Millimeter data for IP Tau and T56 are from Andrews & Williams (2005) and Henning et al. (1993), respectively. (A color version of this figure is available in the online journal.)

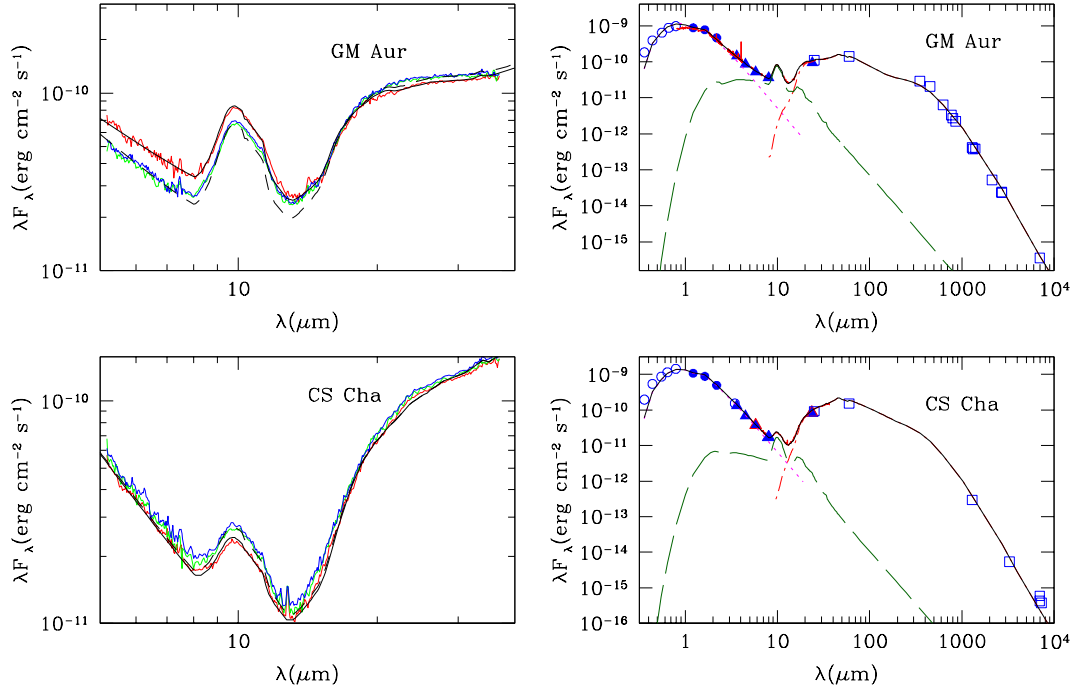


Figure 16. SEDs and disk models of GM Aur and CS Cha. The left panels show the IRS GTO (red), GO1 (green), and GO2 (blue) spectra for the target plotted with the best fit models (solid and broken black lines; refer to the Appendix for more details). Data are the same as listed in Figure 10. SpeX spectra first presented in Espaillat et al. (2010) are also plotted in the case of GM Aur. Millimeter data for GM Aur were obtained from Andrews & Williams (2005); Weintraub et al. (1989); Beckwith & Sargent (1991); Dutrey et al. (1998); Koerner et al. (1993); Looney et al. (2000); Rodmann et al. (2006); Hughes et al. (2009). Millimeter fluxes for CS Cha are from Weaver & Jones (1992); Henning et al. (1993); Lommen et al. (2007, 2009). (A color version of this figure is available in the online journal.)

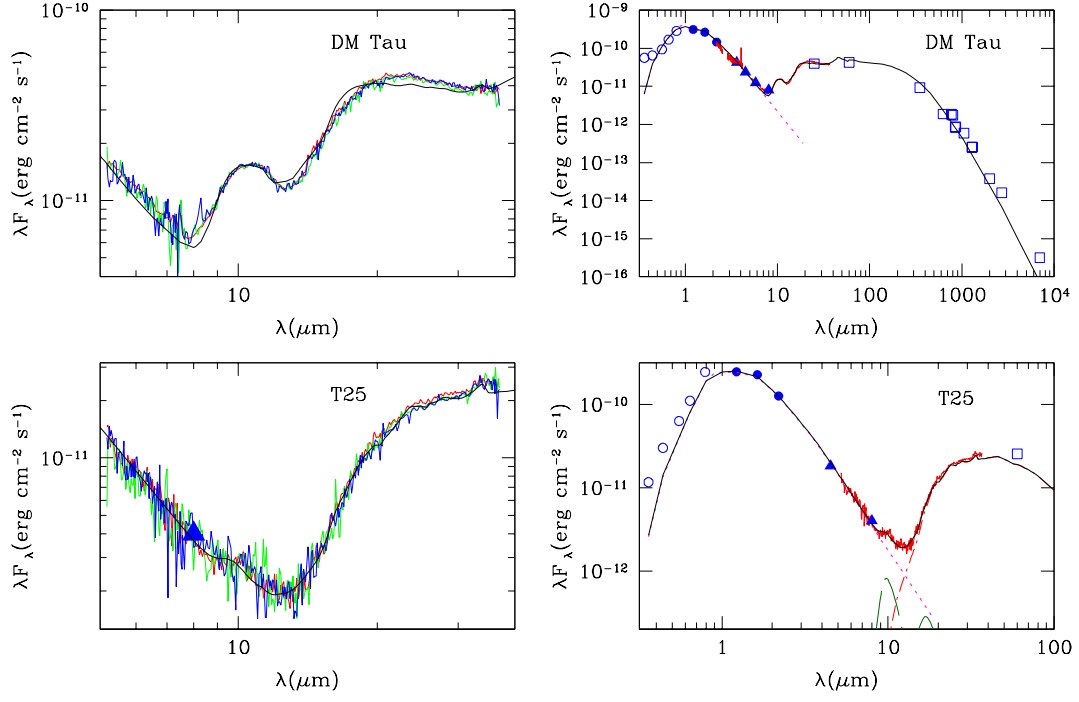


Figure 17. SEDs and disk models of DM Tau and T25. The left panels show the IRS GTO (red), GO1 (green), and GO2 (blue) spectra for the target plotted with the best fit models (solid and broken black lines; refer to the Appendix for more details). Refer to the caption of Figure 10 for more details on the plotted data. SpX spectra first presented in Espaillat et al. (2010) are also plotted for DM Tau. Millimeter data for DM Tau are taken from Andrews & Williams (2005, 2007); Rodmann et al. (2006); Kitamura et al. (2002); Dutrey et al. (1996); Beckwith et al. (1990); Beckwith & Sargent (1991). (A color version of this figure is available in the online journal.)

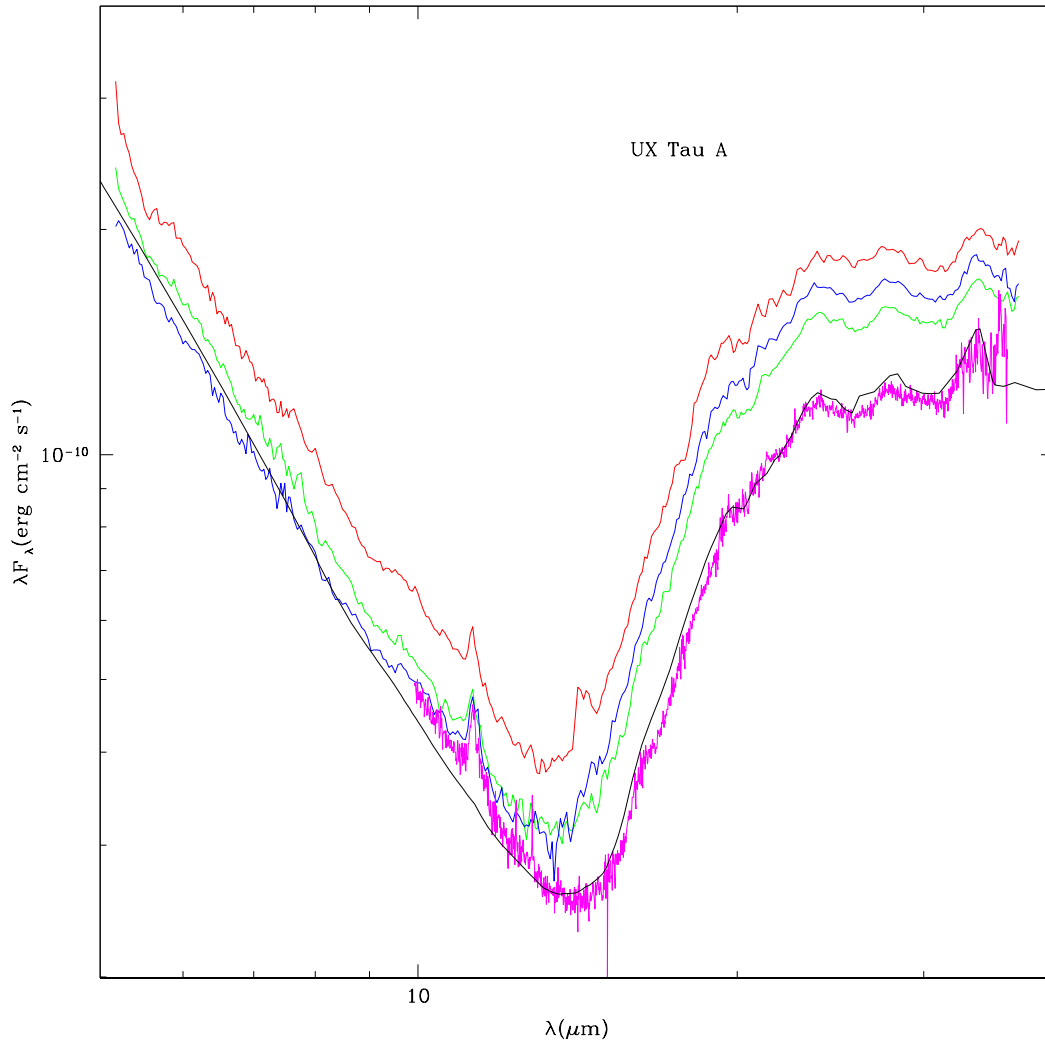


Figure 18. SHLH spectrum and disk model fit for UX Tau A. Here we show the IRS GTO (red), GO1 (green), and GO2 (blue) spectra for UX Tau A from Figure 10 plotted with the unbinned SHLH spectrum (magenta). The best fit model to the SHLH spectrum is shown (solid black line; refer to the Appendix for more details). See Figure 10 for model fits to the GO1 and GO2 spectra. (A color version of this figure is available in the online journal.)